

## Article

# Rare and Critical Metals in Pyrite, Chalcopyrite, Magnetite, and Titanite from the Vathi Porphyry Cu-Au±Mo Deposit, Northern Greece

Christos L. Stergiou <sup>1,\*</sup>, Vasilios Melfos <sup>1,\*</sup>, Panagiotis Voudouris <sup>2</sup>, Lambrini Papadopoulou <sup>1</sup>, Paul G. Spry <sup>3</sup>, Irena Peytcheva <sup>4</sup>, Dimitrina Dimitrova <sup>4</sup>, Elitsa Stefanova <sup>4</sup> and Katerina Giouri <sup>1</sup>

- <sup>1</sup> Faculty of Geology, Aristotle University of Thessaloniki, 54124 Thessaloniki, Greece; lambrini@geo.auth.gr (L.P.); agiouri@geo.auth.gr (K.G.)
- <sup>2</sup> Faculty of Geology and Geoenvironment, National and Kapodistrian University of Athens, 15784 Athens, Greece; voudouris@geol.uoa.gr
- <sup>3</sup> Department of Geological and Atmospheric Sciences, Iowa State University, Ames, IA 50011-1027, USA; pgspry@iastate.edu
- <sup>4</sup> Geological Institute, Bulgarian Academy of Sciences, 241113 Sofia, Bulgaria; irena.peytcheva@erdw.ethz.ch (I.P.); didi@geology.bas.bg (D.D.); elitsas@intern.ethz.ch (E.S.)
- \* Correspondence: christer@geo.auth.gr (C.L.S.); melfosv@geo.auth.gr (V.M.)



**Citation:** Stergiou, C.L.; Melfos, V.; Voudouris, P.; Papadopoulou, L.; Spry, P.G.; Peytcheva, I.; Dimitrova, D.; Stefanova, E.; Giouri, K. Rare and Critical Metals in Pyrite, Chalcopyrite, Magnetite, and Titanite from the Vathi Porphyry Cu-Au±Mo Deposit, Northern Greece. *Minerals* **2021**, *11*, 630. <https://doi.org/10.3390/min11060630>

Academic Editor: Liqiang Yang

Received: 24 May 2021

Accepted: 11 June 2021

Published: 14 June 2021

**Publisher's Note:** MDPI stays neutral with regard to jurisdictional claims in published maps and institutional affiliations.



**Copyright:** © 2021 by the authors. Licensee MDPI, Basel, Switzerland. This article is an open access article distributed under the terms and conditions of the Creative Commons Attribution (CC BY) license (<https://creativecommons.org/licenses/by/4.0/>).

**Abstract:** The Vathi porphyry Cu-Au±Mo deposit is located in the Kilkis ore district, northern Greece. Hydrothermally altered and mineralized samples of latite and quartz monzonite are enriched with numerous rare and critical metals. The present study focuses on the bulk geochemistry and the mineral chemistry of pyrite, chalcopyrite, magnetite, and titanite. Pyrite and chalcopyrite are the most abundant ore minerals at Vathi and are related to potassic, propylitic, and sericitic hydrothermal alterations (A- and D-veins), as well as to the late-stage epithermal overprint (E-veins). Magnetite and titanite are found mainly in M-type veins and as disseminations in the potassic-calcic alteration of quartz monzonite. Disseminated magnetite is also present in the potassic alteration in latite, which is overprinted by sericitic alteration. Scanning electron microscopy and laser ablation inductively coupled plasma mass spectrometry (LA-ICP-MS) analyses of pyrite and chalcopyrite reveal the presence of pyrrhotite, galena, and Bi-telluride inclusions in pyrite and enrichments of Ag, Co, Sb, Se, and Ti. Chalcopyrite hosts bornite, sphalerite, galena, and Bi-sulfosalt inclusions and is enriched with Ag, In, and Ti. Inclusions of wittichenite, tetradymite, and cuprobismutite reflect enrichments of Te and Bi in the mineralizing fluids. Native gold is related to A- and D-type veins and is found as nano-inclusions in pyrite. Titanite inclusions characterize magnetite, whereas titanite is a major host of Ce, Gd, La, Nd, Sm, Th, and W.

**Keywords:** rare metals; critical metals; rare-earth elements; porphyry deposit; Vathi; Serbo-Macedonian metallogenic province; mineral chemistry; hydrothermal alteration zones; LA-ICP-MS

## 1. Introduction

The group of rare metals includes Ag, Au, Be, Bi, Cd, Ce, Co, Ga, Ge, Hg, In, Li, Nd, Rb, Re, Sc, Se, Sr, Ta, Te, Th, U, V, W, Y, the REE-lanthanides, and the platinum group elements (PGE) [1–4]. These metals are characterized by low concentrations in various rock types and deposits, resulting in scarce occurrences of economically valuable concentrations [1–4]. The term “rare” metals is usually coupled with the terms “critical” or “strategic” metals, and the elements included in both groups largely overlap [2,3]. Rarity is a prominent geological factor while criticality reflecting industrial and market values and is defined by the importance of a specific metal to the high-technological industrial sector and by demand and supply [4]. Thus, the list of critical metals is subject to periodic assessment and review [4]. The 2020 European Union critical raw materials (CRM) list includes the following metals: Be, Bi, Co, Ga, Ge, Hf, In, Li, Nb, Sb, Sc, Sr, Ta, Ti, V, W, REE, and PGE [5].

Major deposits of rare metals are generally related to alkaline/peralkaline-carbonatite igneous rocks (e.g., carbonatites and granitic pegmatites), to sedimentary phosphorite and uranium ores, and to placer-type REE deposits [1,6–8]. However, deposits formed by magmatic-hydrothermal processes including porphyry Cu-Mo and epithermal gold deposits related to alkaline igneous rocks, as well as Carlin-type and orogenic gold deposits, are also potential sources of rare metals, mainly as by-products [9–12].

Pyrite and chalcopyrite are common sulfides in various types of metallic mineralization, whereas magnetite and titanite are common accessories and, therefore, have been used as indicator minerals for specific ore types [13–26]. Over the last 20 years, several studies have utilized the trace element compositions of these minerals, in an attempt to interpret the ore-forming processes related to rare metal exploration [13–26].

In porphyry-type deposits, pyrite is ubiquitous in the potassic, propylitic, and sericitic alterations related to disseminations and to vein-style mineralization (A, B and D types) [27]. The A-type veins exhibit sinuous to planar shapes, ranging from stockworks to subparallel sheeted arrays [27]. They primarily consist of quartz, magnetite, chalcopyrite, and bornite [27]. The B- and D-type veins are planar in shape. The B-type veins contain mostly quartz, molybdenite, chalcopyrite, and pyrite, while the D-type veins host quartz, pyrite, and chalcopyrite [27]. Pyrite also occurs in epithermal or E-type veins related to the porphyry–epithermal transition environment [28]. This type of vein occurs in the periphery of the porphyry system and is described by epithermal affinities [22,28]. These veins can accommodate a variety of sulfides including enargite, fersmanite, sphalerite, and galena and they are usually rimmed by quartz and calcite [28]. Chalcopyrite is mined for Cu, but Ag is also extracted as a by-product [14,27]. With respect to hydrothermal alterations and vein-style mineralization in porphyry systems, chalcopyrite exhibits a distribution similar to pyrite, but it is generally absent in propylitic alteration [16]. The study of magnetite and titanite in the porphyry deposits serves as a potential exploration tool for Au-rich ore zones and can help discriminate barren from mineralized intrusions [16,17,23,29–33]. They are associated with the potassic and sodic-calcic alterations, where they are found as disseminations and occur in M-, A-, and B-type veins [27,30,32]. The M-type veins are planar in shape and contain predominantly magnetite [27,30].

In Greece, mining for base (e.g., Cu, Pb, Zn) and precious metals (e.g., Au, Ag) dates back to the prehistoric period and was very intense during Classical times [34,35]. Galena, sphalerite, and gold-bearing pyrite and arsenopyrite are still mined actively in northern Greece, while recent exploration for Cu, Au, and Ag has raised new possibilities for their exploitation [36]. The Serbo-Macedonian Massif (SMM) in northern Greece is characterized by the Vertiskos Unit and hosts several porphyry systems that were formed during the Cenozoic, as a result of the closure of the Western Tethyan Ocean [37,38]. They occur in the Kilikis and NE Chalkidiki ore districts (Figure 1). The SMM, along with the adjacent Rhodope Massif, is a potential region for future exploration of rare metals [3,22,23,39–50].

The tectonic setting, magmatism, hydrothermal alteration, ore mineralogy, and fluid inclusion of the Vathi porphyry Cu-Au±Mo deposit in the Kilikis district were previously studied by Filippidis et al. [51], Frei [52], and, most recently, Stergiou et al. [53]. In addition, a soil geochemical investigation was carried out by Kelepertsis et al. [54]. However, the distribution, abundance, and correlation of rare metals among the different hydrothermal alteration styles and mineralization stages have not been evaluated previously. In the present study, emphasis is given to the distribution of the rare metals including Ag, Au, Bi, Ce, Co, Ga, Gd, Ge, In, La, Nb, Nd, Se, Sm, Ta, Te, Th, U, and W, in pyrite, chalcopyrite, magnetite, and titanite. For these trace elements, we review previous and new bulk geochemical analyses. The trace element composition of these minerals was determined by LA-ICP-MS analyses, and the concentrations and distribution of the rare metals were subsequently evaluated using Pearson's correlation. The results illuminate the metal endowment of the hydrothermal fluids related to the precipitation of the studied minerals.

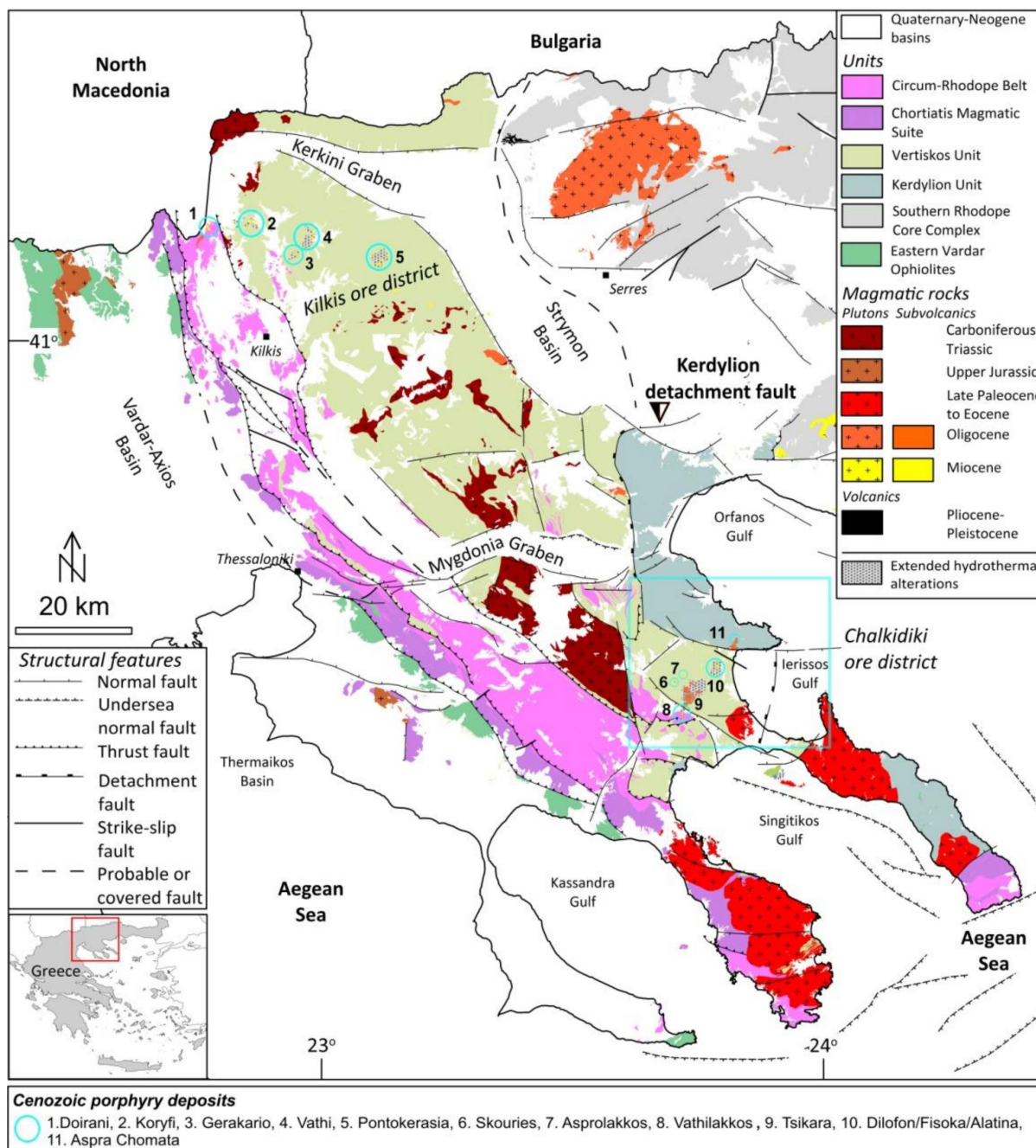


**Figure 1.** The geological setting of the Cenozoic magmatic rocks and related porphyry-type mineralization of the Vertiskos Unit (modified after [35,38,42,53,55,56]).

## 2. Geological Setting

### 2.1. Regional Geology

The Vertiskos Unit is an NW-trending polytectonic and polymetamorphosed geotectonic and basement zone, stretching from the Greek–North Macedonian border to the Chalkidiki peninsula [57–61] (Figure 1). It consists of gneisses, schists, and amphibolites intercalated with marble. Metagabbros–metadiabases and A-type granites of the Paleozoic to Triassic ages are also present [58,59,62]. The Cenozoic igneous evolution is characterized by four magmatic pulses spanning from the Late Paleocene to the Pliocene and includes I-type plutonic, sub-volcanic, and volcanic rocks, associated with calc-alkaline to high-K-calcalkaline and shoshonitic affinities [56,62] (Figure 1). The second and the third magmatic

pulses (Oligocene–Miocene) are related to mineralized intrusions, located mainly in the Kilkis and the NE Chalkidiki ore districts [37,53,56] (Figure 1).

The Vertiskos Unit is located in the hanging wall of the Eocene–Oligocene Kerdylion first-order detachment fault, while another first-order structure of the region is the Miocene Strymon detachment fault exposed mainly in SW Bulgaria [57,60]. These two detachment faults are associated with an extensional regime, lasting from the Late Cretaceous to the Miocene, and which resulted in the collapse of the Vertiskos Unit towards the SSW [55–60]. In the Vertiskos Unit, the extension is documented by ENE–WSW- and eastward-trending shears and related to E–W-, NW–SE-, and NE–SW-trending normal to oblique faults and N–S-trending strike-slip faults [56,58]. The Cenozoic magmatic events and the formation of the Oligocene–Miocene mineralized intrusions were structurally controlled by these faults [53,56].

## 2.2. The Vathi Deposit

The Kilkis ore district, in the northern part of the Vertiskos Unit, includes several porphyry prospects at Vathi, Pontokerasia, Koryfi, Doirani, and Gerakario [37,38,53] (Figure 1). The Vathi porphyry deposit (N41.1458°, E22.9639°) is located near Vathi village, along Ragian Hills 1 and 2 [53] (Figure 2). Exploration projects during the 1970s and the 1980s indicated estimates of more than 258 Mt of ore with 0.40 wt.% Cu and 0.9 g/t Au [37,63].

The mineralization is hosted by latite and is genetically associated with a quartz monzonite ( $18 \pm 0.5$  Ma and  $17 \pm 1$  Ma; U–Pb zircon ages) [52,53], which intruded the crystalline basement rocks and the latite (Figure 2). Both magmatic rocks are silica-saturated and exhibit calc-alkaline to slightly alkaline chemical affinities [52,53]. A phreatic breccia crosscuts the latite and is genetically related to the quartz monzonite intrusion, whereas a latite cataclasite located in the northern part of Ragian Hill 1 is associated with a late epithermal event [53] (Figure 2). Old exploration drilling projects at Vathi revealed the development of a ~100 m-deep oxidation zone, and a narrow secondary enrichment zone [53].

Quartz monzonite outcrops are rare but are characterized by a weak potassic alteration, whereas the latite was affected by a local propylitic alteration. An intense sericitic alteration overprinted these two alteration styles [51–53]. Locally, a subsequent epithermal overprint is observed in the latite. Mineralization forms disseminations, aggregates, and veins (M, A, and D types), while the metallic assemblage related to the epithermal overprint is accommodated in E-type veins [53].

The porphyry-style mineralization was developed in a shallow (<2.6 km in depth) environment from hydrothermal fluids with moderate to high salinities at a minimum temperature of 311 °C. The late epithermal overprint was associated with less saline fluids (1.4–2.9 wt.% NaCl equiv.) and lower temperatures ranging from 205 to 259 °C [53]. Surface samples contain as much as 9297 ppm Cu, 341 ppm Mo, 7 ppm Au, and 263 ppm U. In addition, an enrichment of La (up to 613 ppm), Ce (up to 894 ppm), and Nd (up to 211 ppm) is attributed to the formation of phreatic breccia [53].

## 2.3. Mineralization Stages and Alteration Styles

Early- to late-stage hydrothermal vein types at Vathi correspond to potassic-calcic (M-type), potassic (A-type), and sericitic (D-type) alterations [53], whereas E-type veins are associated with the late epithermal stage (Figure 3a,b,d–g). Potassic alteration is overprinted by sericitic alteration (Table 1). The following ore mineral assemblages are present: (1) magnetite associated with potassic-calcic alteration, (2) magnetite + pyrite + chalcopyrite ± molybdenite ± bornite related to potassic alteration, (3) pyrite + chalcopyrite associated with propylitic alteration, (4) pyrite + chalcopyrite + galena + sphalerite + native gold + tetradymite related to sericitic alteration, and (5) sphalerite + galena + arsenopyrite + pyrrhotite + pyrite + tetrahedrite ± stibnite ± tennantite associated with the epithermal overprint.

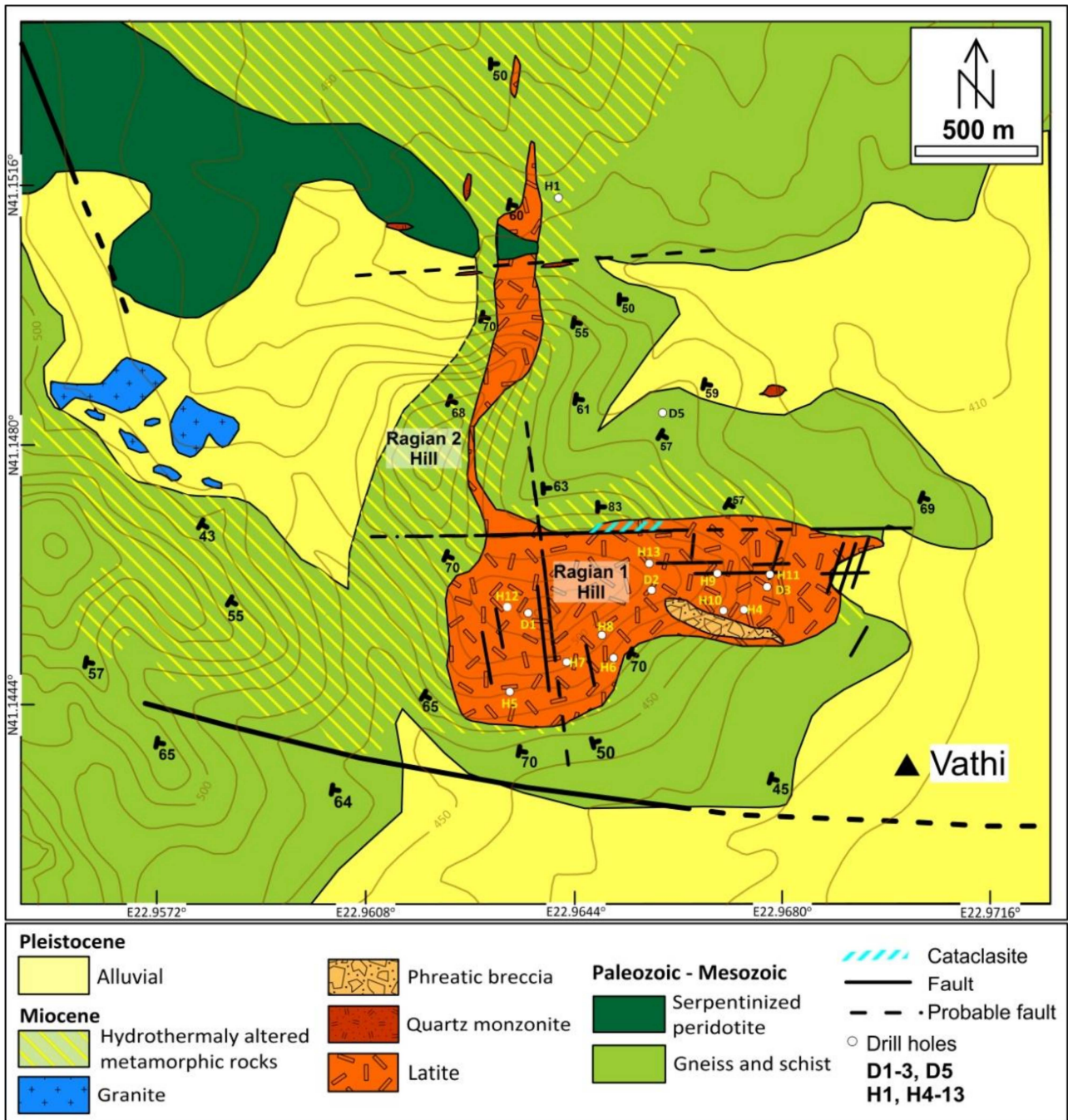
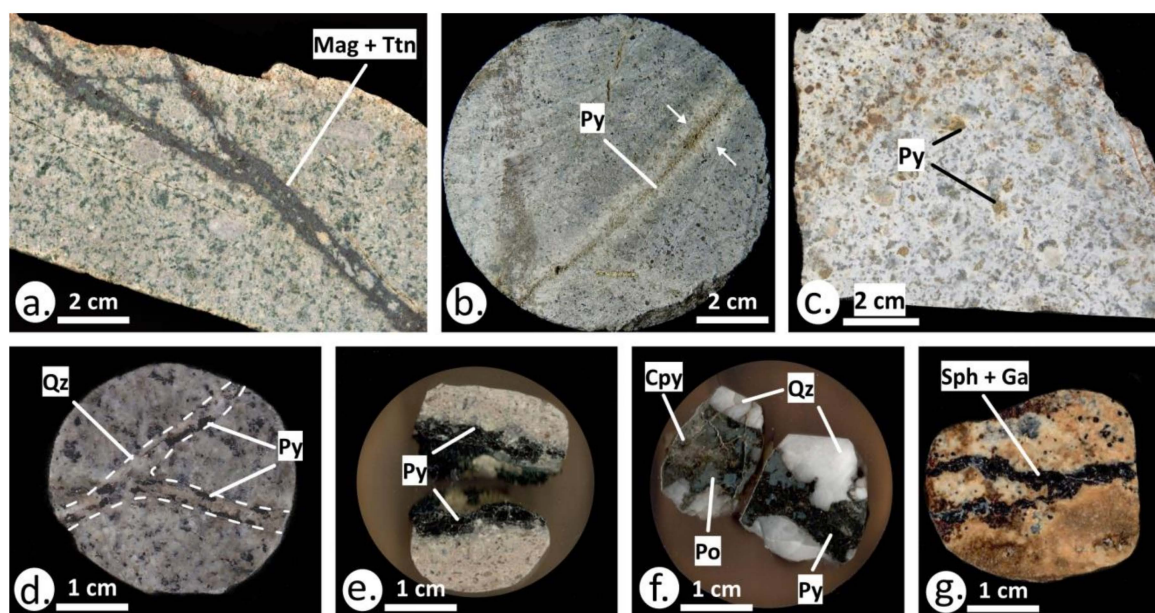


Figure 2. Geological map of the Vathi porphyry system. The legacy drill holes are also shown (modified after [53]).



**Figure 3.** Mineralization stages from the Vathi porphyry Cu-Au-(Mo) system. (a) Magnetite (Mag) and titanite (Ttn) in M-type vein crosscutting a quartz monzonite surface sample (potassic-calcic alteration); (b) pyrite (Py) in A-type vein crosscutting quartz monzonite drill core sample (potassic overprinted by sericitic alteration). A distinctive hydrothermal halo envelopes the vein (white arrows); (c) disseminations and aggregates of pyrite (Py) in a latite surface sample (sericitic alteration); (d) quartz (Qz) and pyrite (Py) in a D-type vein from a quartz monzonite surface sample (sericitic alteration); (e) pyrite (Py) in D-type vein from a latite drill core sample (sericitic alteration); (f) pyrite (Py), pyrrhotite (Po), and chalcopyrite (Cpy) in E-type vein from a latite drill core sample (epithermal overprint); (g) sphalerite (Sph) and galena (Gn) in E-type vein from a latite drill core sample (epithermal overprint).

**Table 1.** Typology, alteration, and textural characteristics of the studied mineralization stages from the Vathi porphyry deposit.

Alteration Style	Host Rock	Mineralization Stage	Metallic Assemblage	Alteration Assemblage
Potassic-calcic	Quartz monzonite	M-type veins Disseminated	Mag ± Ilm	Qz + Bt + Ttn + Act + Rt ± Chl
Potassic (overprinted by sericitic)	Quartz monzonite	A-type veins	Py + Cpy + Au ± Bn ± Gn	Qz + Bt + Kfs + Chl + Ser ± Rt
	Latite	Disseminated	Mag + Py + Cpy ± Bn ± Mol ± Po	
Sericitic	Quartz monzonite	D-type veins	Py + Cpy + Gn + Au + Ttd	Ser + Qz + Rt ± Dol ± Kln
		D-type veins	Py ± Cpy	
	Latite	Disseminated	Py + Cpy + Gn + Sph + Au ± Bn ± Mol ± Po ± Pn ± Tnt ± Ttr ± Wt ± Flt ± Cup ± Sch	
Propylitic	Quartz monzonite	Disseminated	Py	Chl + Qz ± Cal ± Ep
	Latite		Py ± Cpy	
Epithermal	Latite	E-type veins	Assemblage 1: Sph + Gn + Apy + Py + Cpy + Ttr ± Tnt ± Stb Assemblage 2: Py + Po + Cpy ± Gn	Qz + Prl

Mineral abbreviations: Act = actinolite, Apy = arsenopyrite, Au = native gold, Bn = bornite, Bt = biotite, Cal = calcite, Chl = chlorite, Cpy = chalcopyrite, Cup = cuprobismutite, Dol = dolomite, Ep = epidote, Flt = fletcherite, Gn = galena, Ilm = ilmenite, Kfs = K-feldspar, Kln = kaolinite, Mag = magnetite, Mol = molybdenite, Pn = Pentlandite, Po = pyrrhotite, Prl = pyrophyllite, Py = pyrite, Qz = quartz, Rt = rutile, Sch = scheelite, Sph = sphalerite, Stb = stibnite, Ttn = titanite, Tnt = tennantite, Ttd = tetradymite, Ttr = tetrahedrite, Wt = wittichenite.

Potassic-calcic alteration occurs in the quartz monzonite and is characterized by disseminations and M-type veins. These veins are up to 1 cm wide, continuous, sharp-edged, and branched (Figure 3a). They exhibit a massive texture and consist mainly of magnetite and titanite (Figure 4a). This hydrothermal alteration is characterized by quartz, biotite, titanite, actinolite, rutile, and minor ilmenite and chlorite (Table 1).

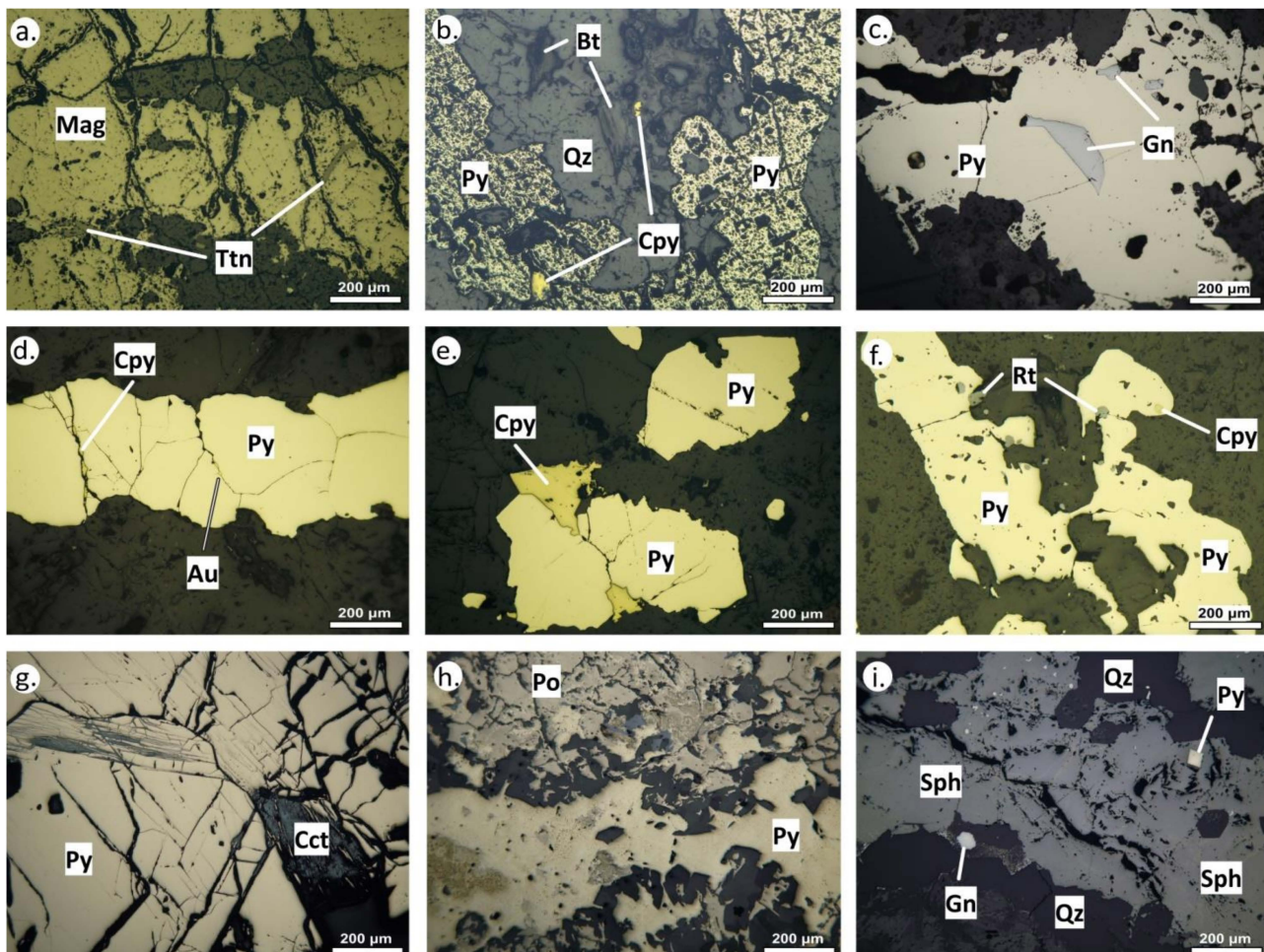


**Figure 4.** Photomicrographs (plane reflected light) of the hypogene mineralization in quartz monzonite (a–e) and latite (f–i): (a) magnetite (Mag) and titanite (Ttn) in M-type vein from potassic-calcic alteration; (b) pyrite (Py), chalcopyrite (Cpy), quartz (Qz), and biotite (Bt) in A-type vein from potassic alteration with sericitic overprint; (c) pyrite (Py) in a D-type vein and galena (Gn) filling interstices; disseminated mineralization with pyrite (Py) and galena (Gn) in sericitic alteration; (d) pyrite (Py), chalcopyrite (Cpy), and native gold (Au) in D-type vein in sericitic alteration; (e) disseminated mineralization with pyrite (Py) and chalcopyrite (Cpy) found in the rock mass around the D-type vein (sericitic alteration); (f) pyrite (Py) aggregates with inclusions of chalcopyrite (Cpy) in sericitic alteration; rutile (Rt) is present near the pyrite–host rock contact; (g) pyrite (Py) and secondary chalcocite (Cct) in a D-type vein in sericitic alteration; (h) pyrrhotite (Po) and pyrite (Py) intergrown in E-type vein (epithermal overprint); (i) sphalerite (Sph), galena (Gn), and euhedral pyrite (Py) in E-type vein rimmed by quartz (Qz) (epithermal overprint).

Potassic alteration affected both the quartz monzonite and latite. A-type veins are up to 2 cm wide, continuous, and enveloped by a hydrothermal halo (Figure 3b). They consist of pyrite, chalcopyrite (Figure 4b), native gold, and traces of bornite and galena [53]. In the latite, disseminated magnetite, pyrite, and chalcopyrite, with minor bornite, molybdenite, and pyrrhotite, are found. The alteration assemblage includes quartz, biotite, K-feldspar, and minor chlorite, sericite, and rutile (Table 1).

Sericitic alteration is associated with disseminations and D-type veins (Figure 3c). In the quartz monzonite, D-type veins are up to 5 cm wide continuous, sharp-edged, and

branched in shape (Figure 3d,e). They consist of pyrite, chalcopyrite, and galena (Figure 4c). In minor amounts, native gold (Figure 4d) and tetradymite are found. These minerals also occur as disseminations around the D-type veins. In the latite, the disseminated mineralization consists of pyrite, chalcopyrite, galena, sphalerite, and native gold, and traces of bornite, molybdenite, pyrrhotite, pentlandite, tennantite, tetrahedrite, wittichenite, fletcherite, cuprobismutite, and scheelite, while the D-type veins host pyrite and minor chalcopyrite (Table 1; Figure 4f,g). Sericitic alteration assemblage includes sericite, quartz, rutile, and minor dolomite and kaolinite (Table 1).

The epithermal overprint is characterized by E-type veins, which are continuous (< 2 cm in width) and branched (Figure 3f,g). The E-type veins host two distinct metallic assemblages consisting of: (1) sphalerite, galena, arsenopyrite, pyrite, chalcopyrite, and tetrahedrite, with minor stibnite and tennantite, and (2) pyrite, pyrrhotite, chalcopyrite, and traces of galena (Table 1; Figure 4h,i). Quartz and pyrophyllite are the characteristic hydrothermal minerals associated with metallic mineralization (Table 1; [53]).

### 3. Materials and Methods

Ten surface samples from the Vathi deposit were collected, with a focus on hydrothermal alteration styles and mineralization stages. In addition, a set of eight older surface samples and 16 drill core samples were evaluated for further mineralogical and geochemical study. The core samples are from two legacy exploration drilling projects that targeted the uranium and the porphyry-style mineralization conducted during the 1970s and 1980s [53]. Eight polished sections studied here were from drill core H4 (43 to 166 m interval), and seven were from drill core H5 (53 and 73 m interval) (Figure 2). Description and characterization of the mineralogy and the alteration styles of the available drill cores can be found in Stergiou et al. [53].

Bulk geochemical analyses of eight samples were conducted for trace elements, including REE, by inductively coupled plasma atomic emission spectroscopy (ICP-AES) at MSALABS, Langley, Canada. Additionally, 19 previously published geochemical analyses were considered in this study (see Supplementary Table S1; [53]).

The samples were studied with an optical microscope and a JEOL JSM-840A scanning electron microscope (SEM) equipped with an OXFORD INCA 300 energy-dispersive system (EDS) (Oxford Instruments Ltd., Abingdon, UK) at the Faculty of Sciences, Aristotle University of Thessaloniki. The operating conditions were a 20 kV accelerating voltage and 0.4 mA probe current, 80 s analysis time, and a beam diameter of  $\approx 1 \mu\text{m}$ , in the back-scattering electron (BSE) mode. Internal empirical corrections were performed to compensate for peak overlap. SEM-EDS micro-analyses were conducted for the determination of iron and titanium contents used as internal standards in LA-ICP-MS analyses for pyrite, chalcopyrite, magnetite, and titanite (see Supplementary Table S2).

Following electron microscopy study, seven polished sections from the drill core samples and three from surface samples were selected to be analyzed by LA-ICP-MS. Trace element concentrations in pyrite, chalcopyrite, magnetite, and titanite were measured using a PerkinElmer ELAN DRC-e ICP mass spectrometer combined with a New Wave UP193-FX excimer laser ablation system at the Geological Institute, Bulgarian Academy of Sciences, Sofia, Bulgaria. The ablation was conducted in He medium. In order to maximize sensitivity, the ICP-MS was optimized daily with respect to the oxide production rate of ThO/Th (0.5%). Operating conditions of the laser system include: 5 Hz repetition rate; 20 to 50  $\mu\text{m}$  spot size; and energy density on analyzed minerals and standards of 5.0 J/cm<sup>2</sup> (at 35 and 50  $\mu\text{m}$  spot) and 4.5 J/cm<sup>2</sup> (at 25 and 20  $\mu\text{m}$  spot). The nebulizer gas flow rate was 0.8 L/min, while auxiliary and make-up gas flows rates were 0.92 L/min. The analysis time was 100 s (background: 40 s, laser—on the sample: 60 s). The acquisition dwell time was set to 0.02 s for <sup>74</sup>Ge, <sup>82</sup>Se, <sup>115</sup>In, <sup>125</sup>Te, and <sup>202</sup>Hg, to 0.03 s for <sup>107</sup>Ag, to 0.04 s for <sup>197</sup>Au, and to 0.01 s for all other elements. The monitored isotopes include: <sup>27</sup>Al, <sup>31</sup>P, <sup>34</sup>S, <sup>49</sup>Ti, <sup>51</sup>V, <sup>53</sup>Cr, <sup>55</sup>Mn, <sup>57</sup>Fe, <sup>59</sup>Co, <sup>60</sup>Ni, <sup>65</sup>Cu, <sup>66</sup>Zn, <sup>71</sup>Ga, <sup>73</sup>Ge, <sup>74</sup>Ge, <sup>75</sup>As, <sup>77</sup>Se, <sup>93</sup>Nb, <sup>95</sup>Mo, <sup>107</sup>Ag, <sup>111</sup>Cd, <sup>115</sup>In, <sup>118</sup>Sn, <sup>121</sup>Sb, <sup>125</sup>Te, <sup>139</sup>La, <sup>140</sup>Ce, <sup>146</sup>Nd, <sup>147</sup>Sm, <sup>157</sup>Gd, <sup>182</sup>W, <sup>185</sup>Re, <sup>197</sup>Au,

$^{202}\text{Hg}$ ,  $^{205}\text{Tl}$ ,  $^{208}\text{Pb}$ ,  $^{209}\text{Bi}$ ,  $^{232}\text{Th}$ , and  $^{238}\text{U}$ . The targeted areas in the polished sections were predefined to try and avoid mineral inclusions. Repeated external standardization was conducted by analyzing NIST SRM 610 and USGS GSD-1G glass standards, and the USGS Mass 1 sulfide standard.

Data reduction was performed by using the Fe contents of pyrite, chalcopyrite, and magnetite, as well as Ti contents of titanite measured by SEM-EDS as internal standards and the SILLS software [64]. During data reduction, peak-shaped fluctuations of the intensity signal of some isotopes were investigated in order to exclude the influence of other minerals on the chemical composition of the studied minerals. Several elements occur as nano-scale mineral inclusions in pyrite and chalcopyrite and as nanoparticles in magnetite, and in the following, they are described separately. For the full list of the LA-ICP-MS data, including elements ascribed to nano-scale mineral inclusions, see Supplementary Table S3. Additionally, the average detection limits for the analyzed elements are given for each studied mineral in Supplementary Table S3.

For the statistical analysis of the bulk geochemistry and the LA-ICP-MS analytical results, univariate analysis (minimum, maximum, standard deviation, and average) and bivariate analysis (Pearson's correlations) were obtained. The SPSS statistics software (IBM) was used for the statistical analyses. Statistical graphs and time-resolved analytical profiles of LA-ICP-MS analyses were plotted using Grapher software (Golden Software LLC).

## 4. Results

### 4.1. Bulk Geochemistry of Rare and Critical Metals in Metallic Mineralization

Bulk geochemical analysis of mineralized samples was conducted in order to investigate their endowment in rare and critical metals. Eight surface samples were analyzed, five of which were from latite, one was from propylitic alteration (Vath 42), and four were from sericitic alteration (Vath 34, Vath 38, Vath 40, Vath 45). Among the three samples from quartz monzonite, Vath 41 is relatively fresh, while Vath 43 is from a D-type vein in sericitic alteration, and Vath 44 is from an M-type vein in potassic-calcic alteration. Table 2 includes the rare metal concentrations of these samples, and the average values for the same elements from previously published bulk geochemical analyses [53]. The complete analytical datasets for both groups are given in Supplementary Table S1.

**Table 2.** Bulk geochemical analyses of selected rare metals from the Vathi porphyry system. The average values of these elements from previously analyzed samples by Stergiou et al. [53] are also given. For the full list of geochemical analyses, see Table S1 in the Supplementary Materials.

	Latite							Quartz Monzonite				
	Det. limit	Propylitic alteration		Sericitic Alteration				Rel. Fresh	Potassic-Calcic alt.	Sericitic Alteration		
		Vath 42	AVG (n = 3)	Vath 34	Vath 38	Vath40	Vath 45		AVG (n = 16)	Vath 41	Vath 44	Vath 43
ppm												
Ag	0.01	0.45	0.58	0.32	0.48	0.10	0.04	1.1	0.12	0.05	0.89	0.42
Au	0.00005	0.04	0.02	0.07	0.22	0.01	0.004	0.13	0.04	0.01	0.77	0.27
Bi	0.01	4.6	6.5	14.1	0.84	1.4	1.1	21	0.49	0.34	3.4	2.9
Ce	0.02	123	102	121	92	94	31	97	153	62	68	92
Co	0.1	38	13	17	18	48	450	35	23	13	30	45
Ga	0.05	9.4	16	2.2	1.7	1.9	5.1	15	6	7.7	8.5	15
Gd	0.05	6.6	5	4.5	4	4	2.3	5.1	7.8	4.1	3.9	4.7
Ge	0.05	0.24	0.24	0.13	0.11	0.11	0.09	0.11	0.18	0.20	0.19	0.19
In	0.005	0.01	0.11	0.08	0.08	0.05	b.d.l.	0.28	0.01	0.02	0.12	0.27
La	0.2	68	54	64	42	52	18	47	83	27	35	45
Nb	0.05	0.65	8.3	0.22	0.11	0.10	b.d.l.	8.6	1.2	0.6	1.2	5.3
Nd	0.1	46	38	47	35	33	12	40	85	27	28	39
Se	0.2	1.2	1	b.d.l.	3.8	b.d.l.	7.9	3.8	1.2	b.d.l.	2.8	1.8
Sm	0.03	8.1	6.5	7.7	5.7	5.4	2.4	6.9	10	5	4.9	6.8
Ta	0.01	1.4	1.1	b.d.l.	b.d.l.	b.d.l.	b.d.l.	0.84	1.8	b.d.l.	b.d.l.	0.55
Te	0.01	0.49	0.3	0.01	b.d.l.	0.27	0.06	0.17	0.49	0.03	1.5	0.73
Th	0.2	44	45	39	40	36	24	38	68	42	47	46
U	0.05	8.3	9.2	6.1	15	21	6.2	20	16	4.6	20	19
W	0.05	117	49	197	136	122	95	59	181	75	156	80

Abbreviations: AVG = average; n = number of analyses; b.d.l. = below detection limit; Det. limit = detection limit; Rel. Fresh = relatively fresh; Potassic-calcic alt. = potassic-calcic alteration; n.a. = not analyzed.

Potassic-calcic alteration (Vath 44; quartz monzonite) is characterized by a depletion of rare metals (Table 1; Figure 5). Tungsten (75 ppm) is the most enriched rare metal, while Ce (62 ppm), Th (42 ppm), Nd (27 ppm), and La (27 ppm) occur in decreasing concentrations (Table 2).

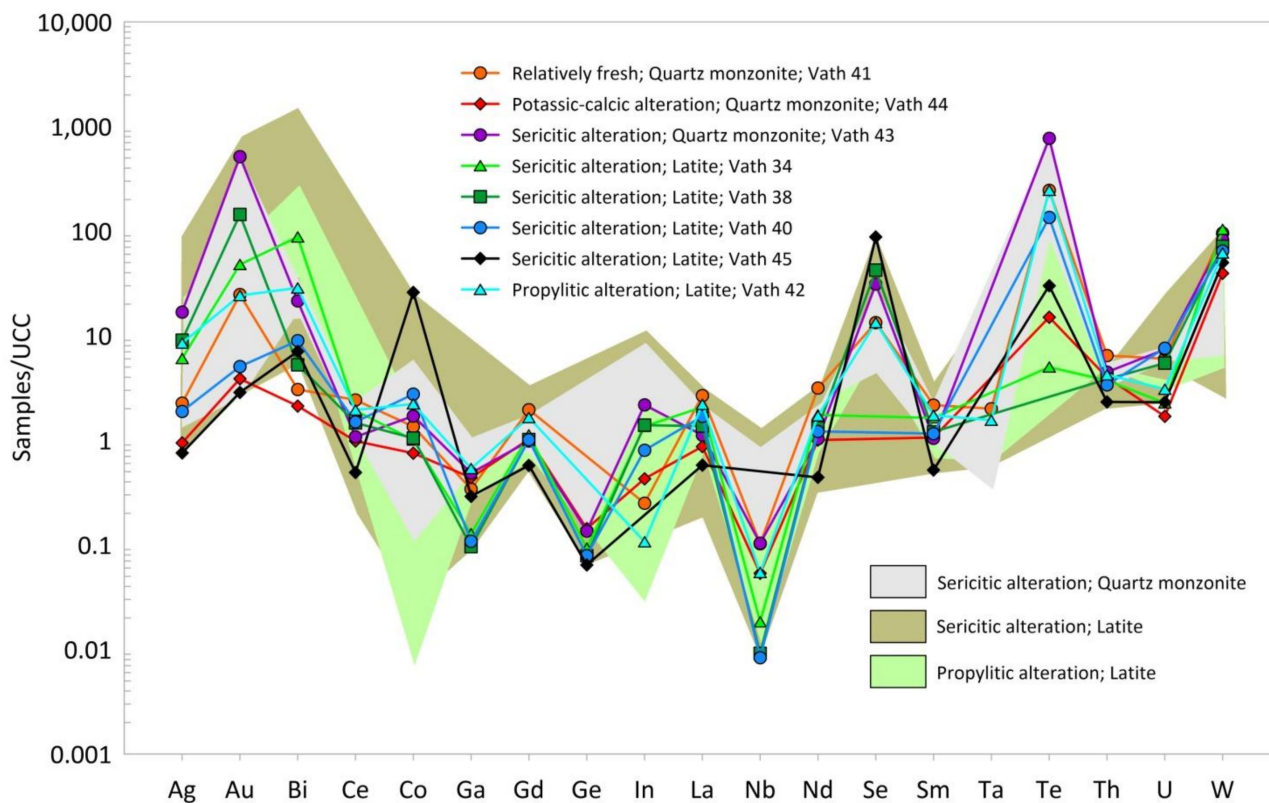


**Figure 5.** Upper continental crust (UCC) normalized logarithmic spider diagram of the eight analyzed samples presented in this study and the plot areas of previously analyzed samples by Stergiou et al. [53] corresponding to sericitic and propylitic alterations of quartz monzonite and latite (UCC normalized values after Rudnick and Gao [65]).

Sericitic alteration is enriched with Au, Bi, Te, Co, Se, and W (Table 1; Figure 5). The quartz monzonite sample Vath 43 is enriched with Au (0.77 ppm) and Te (1.5 ppm). The latite samples (Vath 34 and Vath 45) exhibit the highest concentrations of Bi (14 ppm), Co (450 ppm), Se (8 ppm), and W (197 ppm) (Table 2).

Rare-earth elements are highest in samples Vath 41 and Vath 42 (Figure 5). The relatively fresh quartz monzonite sample (Vath 41) contains significant amounts of Ce (153 ppm), Gd (7.8 ppm), La (83 ppm), Nd (85 ppm), and Sm (10 ppm). In addition, Ta (1.8 ppm) and Th (68 ppm) are more enriched in sample Vath 41 (Table 2).

It is noteworthy that the highest values of Ag (4.6 ppm), Au (7 ppm), and Bi (239 ppm) are related to the D-type veins and the oxidized latite samples from sericitic alteration (Figure 5; Supplementary Table S1; [53]). The highest concentrations of Ce (894 ppm), La (613 ppm), Nd (211 ppm), and Sm (23 ppm) are also related to sericitic alteration and are mainly concentrated in the phreatic breccia (Figure 5; Supplementary Table S1; [53]).

Pearson product-moment correlation coefficients and associated  $p$ -values were calculated for the bulk geochemical analyses conducted in this study along with previously published geochemical analyses (Table 2; Supplementary Tables S1 and S4). The statistical analysis included all the elements listed in Table 1.

Significant positive correlations ( $p < 0.01$ ; values  $\geq 0.822$ ) were obtained for the following elemental pairs: Au–Se, Au–Te, Au–U, Ce–La, Ce–Nd, Ce–Sm, Gd–Nd, Gd–Sm, La–Nd, Nd–Sm, Se–Te, Se–U, and Te–U (Supplementary Table S4). In addition, significant positive correlations ( $p < 0.01$ ; values between 0.495 and 0.781) were defined for

the elemental pairs Ag–Au, Ag–Se, Ag–U, Au–Th, Bi–Gd, Bi–Sm, Ce–Gd, Ce–In, Ga–In, Ga–Nb, Gd–La, Ge–W, In–La, La–Sm, Nb–Ta, Se–Th, Te–Th, and Th–U (Supplementary Table S4). Significant negative correlations ( $p < 0.01$ ; values  $\geq -0.557$ ) occur for the pairs Ga–Ge, Ga–W, Ge–Nb, and Nb–W (Supplementary Table S4).

#### 4.2. Pyrite and Chalcopyrite Mode of Occurrence

Pyrite at Vathi is ubiquitous, especially in potassic and sericitic alterations. It is found as disseminations and aggregates, and in veins (Table 1). In the potassic alteration of the quartz monzonite, pyrite occurs in A-type veins crosscutting the host rock (Figure 4b). It is massive, filling the inner parts of the veins, and is intergrown with chalcopyrite and bornite. Native gold and galena are found in the interstices of pyrite (Figure 6a). In the hydrothermal halo around the A-type veins, pyrite disseminations and aggregates vary in size from 100 to 500  $\mu\text{m}$ . In the potassic alteration of the latite, pyrite (Py1) forms subhedral to euhedral disseminations and rounded aggregates ( $< 1$  mm in size; Figure 6b). It occurs along with magnetite, chalcopyrite, and traces of bornite, molybdenite, and pyrrhotite (Figure 6b).

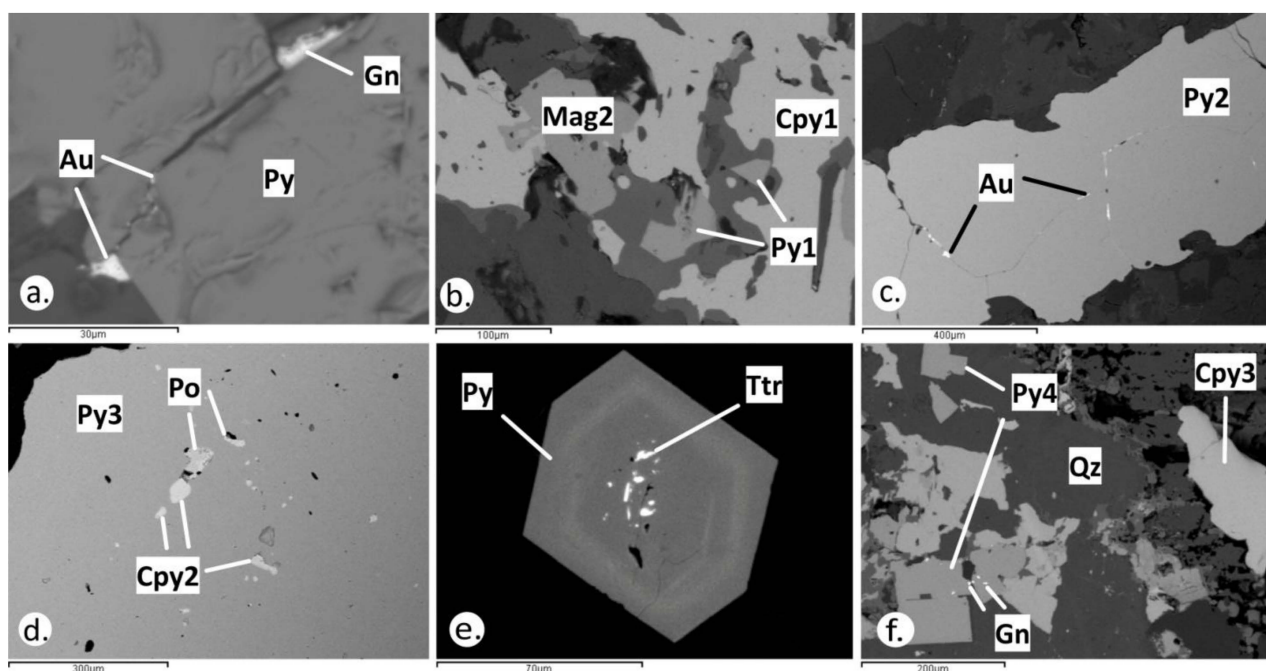


**Figure 6.** SEM back-scattered electron images of pyrite from different mineralization stages from the quartz monzonite (a–d) and the latite (e–i): (a) pyrite (Py), native gold (Au), and galena (Gn) in A-type vein from the potassic alteration; (b) euhedral pyrite (Py1), chalcopyrite (Cpy1), and magnetite (Mag1) from potassic alteration; (c) pyrite (Py2) in D-type vein and native gold (Au) in micro-cracks from sericitic alteration; (d) pyrite (Py3) bearing inclusions of chalcopyrite (Cpy2) and pyrrhotite (Po) from sericitic alteration; (e) euhedral pyrite (Py) bearing tetrahedrite (Ttr) inclusions in E-type vein related to epithermal overprint (assemblage 1); (f) euhedral pyrite (Py4) with galena (Gn) inclusions and chalcopyrite (Cpy3) in quartz (Qz) from E-type vein related to epithermal overprint (assemblage 2).

In the sericitized quartz monzonite, pyrite (Py2) forms subhedral to euhedral disseminations and aggregates varying in size from 50 to 400  $\mu\text{m}$ , and D-type veins (Figures 4c–e and 6c). Pyrite is intergrown with chalcopyrite, galena, native gold, and tetradymite. Galena ( $< 500$   $\mu\text{m}$  in size) is found in interstices or as replacements in disseminated pyrite, while chalcopyrite, native gold (Figures 4d and 6c), and tetradymite are found in micro-cracks and interstices in pyrite filling D-type veins. The sericitic alteration of latite hosts disseminations and aggregates of pyrite as well as massive pyrite in D-type veins (Figure 4f,g). Disseminated pyrite (Py3) is intergrown with chalcopyrite and locally hosts inclusions ( $< 100$   $\mu\text{m}$  in size) of galena and pyrrhotite (Figure 6d; [53]). Pentlandite ( $< 10$   $\mu\text{m}$

in size) was found in pyrrhotite. In D-type veins, massive pyrite is the dominant sulfide, while minor chalcopyrite inclusions are also found.

In the E-type veins related to the epithermal overprint, pyrite is a minor constituent in assemblage 1, and a major constituent in assemblage 2 (Table 1). In assemblage 1, euhedral pyrite (<80  $\mu\text{m}$  in size) is found as inclusions in galena and sphalerite. Locally, it hosts tetrahedrite inclusions (<10  $\mu\text{m}$  in size; Figure 6e). In assemblage 2, massive pyrite (Py4) is intergrown with pyrrhotite filling the inner parts of the veins (Figure 4h). Euhedral pyrite is found in the periphery of the veins and hosts inclusions of galena (Figure 6f).

Chalcopyrite is the second most abundant sulfide in the Vathi deposit (Table 1). In the potassic alteration of the quartz monzonite, chalcopyrite is found in A-type veins along with pyrite, native gold, and minor bornite and galena. In the hydrothermal halo around the A-type veins, chalcopyrite forms disseminations up to 200  $\mu\text{m}$  in size (Figures 4b and 7a). In the potassic alteration of the latite, chalcopyrite (Cpy1; <1 mm in size) overgrew magnetite and coexists with pyrite, bornite, molybdenite, and pyrrhotite (Figures 6b and 7b).

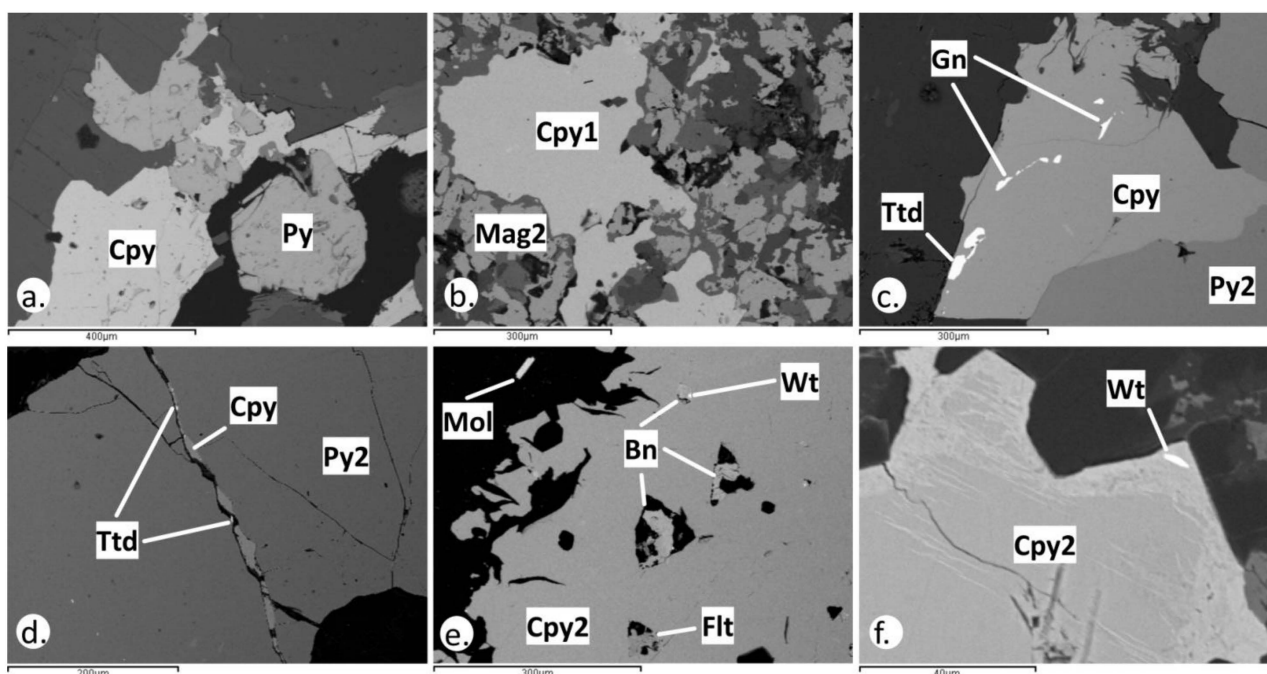


**Figure 7.** SEM back-scattered electron images of chalcopyrite from different mineralization stages from the quartz monzonite (a–c) and the latite (d–f): (a) chalcopyrite (Cpy) is intergrown with pyrite (Py) in A-type vein from potassic alteration; (b) chalcopyrite (Cpy1) overgrowth on magnetite (Mag2) aggregates from potassic alteration; (c) chalcopyrite (Cpy) is intergrown with pyrite (Py2) and bears inclusions of galena (Gn) and tetradymite (Ttd) from sericitic alteration; (d) chalcopyrite (Cpy) and traces of tetradymite (Ttd) fill a crack running across a D-type vein with massive pyrite (Py2) from sericitic alteration; (e) chalcopyrite (Cpy2) and euhedral inclusions of bornite (Bn), fletcherite (Flt), and molybdenite (Mol); traces of wittichenite (Wt) are found in bornite (Bn) from sericitic alteration; (f) chalcopyrite (Cpy2) and wittichenite (Wt) from sericitic alteration.

In the sericitically altered quartz monzonite, chalcopyrite appears as disseminations (<50  $\mu\text{m}$  in size) and as aggregates along with pyrite (Figure 4e). Galena and tetradymite are found as inclusions (<100  $\mu\text{m}$  in size) in chalcopyrite (Figure 7c). In the D-type veins, chalcopyrite occurs in fractures along pyrite (approximately < 50  $\mu\text{m}$  in width; Figures 4e and 7d).

In the sericitic alteration of the latite, chalcopyrite (Cpy2) locally exhibits a more extensive distribution than pyrite and forms large aggregates reaching 1 cm in size. Chalcopyrite hosts inclusions of molybdenite, galena, sphalerite, bornite, pyrrhotite, and pentlandite (< 100  $\mu\text{m}$  in size), as well as native gold, tennantite, tetrahedrite, wittichenite, fletcherite,

and cuprobismutite, which do not exceed 50  $\mu\text{m}$  in size (Figure 7e,f; [53]). In D-type veins, crosscutting the sericitic alteration of latite, chalcopyrite is a minor constituent. It is found in pyrite as inclusions reaching up to 100  $\mu\text{m}$  in size.

In E-type veins, chalcopyrite occurs as nano-scale inclusions in sphalerite (i.e., chalcopyrite disease; assemblage 1; Table 1). In assemblage 2, chalcopyrite (Cpy3) is a minor constituent filling interstices (<100  $\mu\text{m}$ ) between pyrite, pyrrhotite, and quartz (Table 1; Figure 6f).

#### 4.3. Magnetite and Titanite Mode of Occurrence

Magnetite occurs in the potassic-calcic alteration of the quartz monzonite and in potassically altered latite (Table 1). In the potassic-calcic alteration, magnetite (Mag1) occurs as disseminations (<400  $\mu\text{m}$  in size) and in M-type veins (<1 cm in width). It is intergrown with titanite and ilmenite (<100  $\mu\text{m}$  in size; Figure 8a,b). In the M-type veins, massive magnetite is the dominant metallic mineral and includes titanite and ilmenite (Figures 4a and 8c). In the potassic alteration in latite, magnetite (Mag2) occurs as disseminations and aggregates (<500  $\mu\text{m}$  in size; Figures 6b and 7b). It is overgrown by chalcopyrite and hosts minor inclusions of pyrrhotite (<40  $\mu\text{m}$  in size).

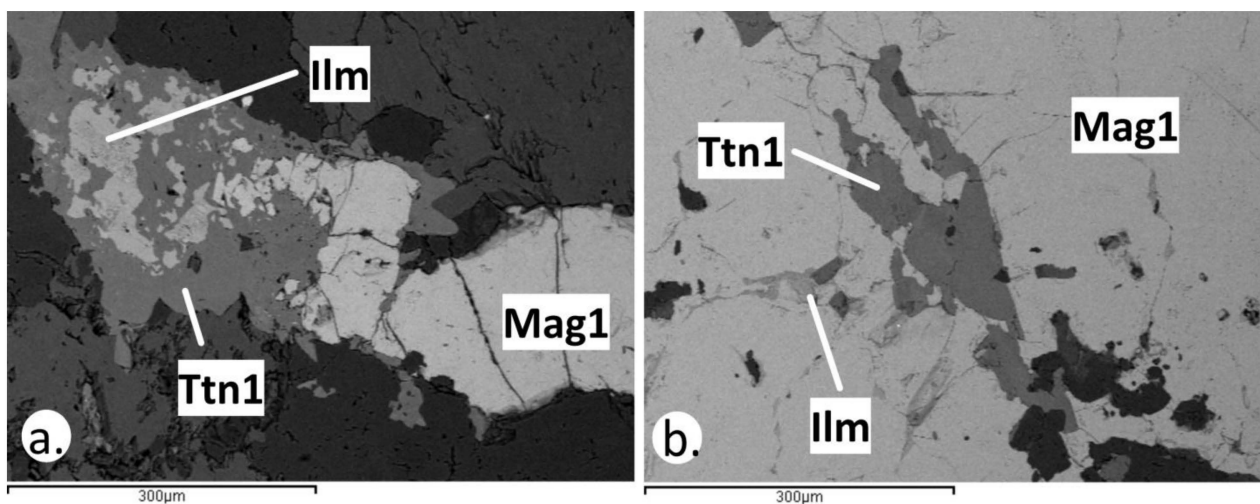


**Figure 8.** SEM back-scattered electron images of magnetite and titanite from different mineralization stages from the potassic-calcic alteration of the quartz monzonite (a,b): (a) disseminated magnetite (Mag1) is intergrown with titanite (Ttn1) and ilmenite (Ilm); (b) massive magnetite (Mag1) including titanite (Ttn1) and ilmenite (Ilm) in M-type vein.

Titanite (Ttn1) is found in the potassic-calcic alteration of the quartz monzonite as disseminations and in M-type veins (Figure 4a). Disseminated titanite (<100  $\mu\text{m}$  in size) appears mainly as subhedral crystals, as intergrowths with ilmenite, and as overgrowths on magnetite. In M-type veins, titanite (<400  $\mu\text{m}$  in size) is included in massive magnetite (Figure 8b).

#### 4.4. Mineral Chemistry

##### 4.4.1. Trace Element Composition of Pyrite and Chalcopyrite

Trace elements in pyrite (Py1, Py2, Py3, Py4) and chalcopyrite (Cpy1, Cpy2, Cpy3) were measured by means of LA-ICP-MS. The trace element composition of pyrite and chalcopyrite exhibits notable variations between the different mineralization stages (Tables 3 and 4; Figure 9). In addition, ablation patterns reveal the occurrence of nano-scale mineral inclusions in pyrite. These inclusions are excluded from Tables 3 and 4. The complete analytical dataset for pyrite and chalcopyrite is given in Supplementary Table S3.

**Table 3.** LA-ICP-MS analyses of pyrite from various mineralization stages. Values are in ppm. For the full dataset, see Supplementary Table S3.

Alteration		Potassic (Overprinted by Sericitic)				Sericitic				Epithermal Overprint							
Host rock		Latite				Quartz monzonite				Latite							
Mineralization stage		Disseminated (n = 9); Py1				D-type veins (n = 9); Py2				Disseminated (n = 19); Py3				E-type veins; assemblage 2 (n = 7); Py4			
Element	MIN	MAX	ST DEV	AVG	MIN	MAX	ST DEV	AVG	MIN	MAX	ST DEV	AVG	MIN	MAX	ST DEV	AVG	
Ti	20.3	39	6.7	29	26	34	2.8	30	20	57	2.6	31	21	41	7	28	
V	9.9	9.9	n.a.	9.9	b.d.l.	b.d.l.	n.a.	n.a.	4.2	4.2	n.a.	4.2	b.d.l.	b.d.l.	n.a.	n.a.	
Cr	27	47	7.9	38	36	46	4	41	31	54	3.8	42	30	42	3.9	35	
Mn	48	91	16	61	53	59	2.3	56	48	76	2.7	55	48	53	2.5	50	
Co	17	1341	409	201	11	93	33	33	0.73	8700	1391	1931	2.3	17,106	7954	4736	
Ni	8.5	9448	3059	1398	4.1	59	22	20	2.3	5406	1411	602	6.2	2153	778	890	
Cu	b.d.l.	b.d.l.	n.a.	n.a.	12	16	1.5	14	4.3	425	139	65	59	59	n.a.	59	
Zn	4.9	8.3	1.4	6.6	6	6.8	0.56	6.4	3.1	9.9	0.24	6.4	3.7	11	4.3	6.4	
As	339	7117	2166	3851	9.7	9.8	0.07	9.7	1.9	469	98	63	4.1	29	9.5	9.4	
Se	11	26	4.4	18	14	19	2.6	16	14	200	27	51	5.8	18	4.9	12	
Mo	b.d.l.	b.d.l.	n.a.	n.a.	b.d.l.	b.d.l.	n.a.	n.a.	2	2	n.a.	2	b.d.l.	b.d.l.	n.a.	n.a.	
Ag	2.2	2.2	n.a.	2.2	0.34	0.65	0.22	0.50	0.34	1.3	0.27	0.67	0.84	6.6	4.1	3.7	
In	0.09	0.09	n.a.	0.09	b.d.l.	b.d.l.	n.a.	n.a.	b.d.l.	b.d.l.	n.a.	n.a.	0.1	0.1	n.a.	0.1	
Sn	b.d.l.	b.d.l.	n.a.	n.a.	b.d.l.	b.d.l.	n.a.	n.a.	0.46	0.46	n.a.	0.46	b.d.l.	b.d.l.	n.a.	n.a.	
Sb	0.34	10	4.8	3.1	2.1	3.23	0.43	2.6	0.45	1.6	0.02	0.96	0.96	1.2	0.2	1.1	
Te	5.3	31	12	15	b.d.l.	b.d.l.	n.a.	n.a.	3	41	n.a.	18	b.d.l.	b.d.l.	n.a.	n.a.	
W	b.d.l.	b.d.l.	n.a.	n.a.	b.d.l.	b.d.l.	n.a.	n.a.	b.d.l.	b.d.l.	n.a.	n.a.	4.4	27	11	12	
Au	b.d.l.	b.d.l.	n.a.	n.a.	b.d.l.	b.d.l.	n.a.	n.a.	b.d.l.	b.d.l.	n.a.	n.a.	b.d.l.	b.d.l.	n.a.	n.a.	
Hg	b.d.l.	b.d.l.	n.a.	n.a.	b.d.l.	b.d.l.	n.a.	n.a.	0.46	0.67	n.a.	0.56	b.d.l.	b.d.l.	n.a.	n.a.	
Tl	0.62	0.67	0.03	0.64	b.d.l.	b.d.l.	n.a.	n.a.	b.d.l.	b.d.l.	n.a.	n.a.	1.2	1.2	n.a.	1.2	
Pb	b.d.l.	b.d.l.	n.a.	n.a.	0.54	4.3	1.9	2.2	b.d.l.	b.d.l.	n.a.	n.a.	7	7	n.a.	7	
Bi	b.d.l.	b.d.l.	n.a.	n.a.	b.d.l.	b.d.l.	n.a.	n.a.	b.d.l.	b.d.l.	n.a.	n.a.	1	1	n.a.	1	

Abbreviations: AVG = average value; b.d.l. = below detection limit; MIN = minimum value; MAX = maximum value; n = number of analyses; n.a. = not analyzed; STDEV = standard deviation.

**Table 4.** LA-ICP-MS analyses of chalcopyrite from various mineralization stages. Values are in ppm. For the full dataset, see Supplementary Table S3.

Alteration		Potassic (Overprinted by Sericitic)				Sericitic				Epithermal Overprint			
Host rock						Latite							
Mineralization stage	Cpy 1; disseminated ( <i>n</i> = 10)				Cpy2; disseminated ( <i>n</i> = 12)				Cpy3; E-type veins; assemblage 2 ( <i>n</i> = 2)				
Element	MIN	MAX	STDEV	AVG	MIN	MAX	STDEV	AVG	MIN	MAX	STDEV	AVG	
Ti	11	41	9.6	24	12	31	6.1	17	45	45	n.a.	45	
V	11	11	n.a.	11	b.d.l.	b.d.l.	n.a.	n.a.	b.d.l.	b.d.l.	n.a.	n.a.	
Cr	20	38	6.7	27	19	55	8.8	29	b.d.l.	b.d.l.	n.a.	n.a.	
Mn	33	40	2.8	36	30	42	1.9	33	31	31	n.a.	31	
Co	4.8	4.9	0.05	4.9	0.58	5.3	2.1	1.7	b.d.l.	b.d.l.	n.a.	n.a.	
Ni	5.1	6.2	0.8	5.7	4.1	7.5	2	5.3	b.d.l.	b.d.l.	n.a.	n.a.	
Zn	137	2392	925	790	19	55	2.1	34	287	571	201	429	
Ga	2.3	2.3	n.a.	2.3	b.d.l.	b.d.l.	n.a.	n.a.	b.d.l.	b.d.l.	n.a.	n.a.	
Ge	b.d.l.	b.d.l.	n.a.	n.a.	4.9	12	5.1	8.5	9	9	n.a.	9	
As	56	83	8.9	67	4.8	25	5.6	12	b.d.l.	b.d.l.	n.a.	n.a.	
Se	b.d.l.	b.d.l.	n.a.	n.a.	46	161	13	73	b.d.l.	b.d.l.	n.a.	n.a.	
Mo	b.d.l.	b.d.l.	n.a.	n.a.	b.d.l.	b.d.l.	n.a.	n.a.	b.d.l.	b.d.l.	n.a.	n.a.	
Ag	6.8	17	3.4	10	8	519	103	47	134	407	193	271	
Cd	4.4	45	15	14	b.d.l.	b.d.l.	n.a.	n.a.	b.d.l.	b.d.l.	n.a.	n.a.	
In	32	62	11	50	3.1	57	8.1	25	1	57	39	29	
Sn	1.8	9	2.9	5.3	18	144	9	119	48	91	31	70	
Sb	b.d.l.	b.d.l.	n.a.	n.a.	1.1	48	26	24	3.4	3.4	n.a.	3.4	
Te	b.d.l.	b.d.l.	n.a.	n.a.	3.9	6.8	1.7	5.1	b.d.l.	b.d.l.	n.a.	n.a.	
W	b.d.l.	b.d.l.	n.a.	n.a.	b.d.l.	b.d.l.	n.a.	n.a.	2	2	n.a.	2	
Au	b.d.l.	b.d.l.	n.a.	n.a.	b.d.l.	b.d.l.	n.a.	n.a.	b.d.l.	b.d.l.	n.a.	n.a.	
Hg	b.d.l.	b.d.l.	n.a.	n.a.	0.83	50	28	17	b.d.l.	b.d.l.	n.a.	n.a.	
Tl	0.42	0.42	n.a.	0.42	38	38	n.a.	38	b.d.l.	b.d.l.	n.a.	n.a.	
Pb	5.4	14	6.1	9.7	4	4	n.a.	4	b.d.l.	b.d.l.	n.a.	n.a.	
Bi	3	40	13	21	2.1	2.1	n.a.	2.1	b.d.l.	b.d.l.	n.a.	n.a.	

Abbreviations: AVG = average value; b.d.l. = below detection limit; MIN = minimum value; MAX = maximum value; n = number of analyses; STDEV = standard deviation.

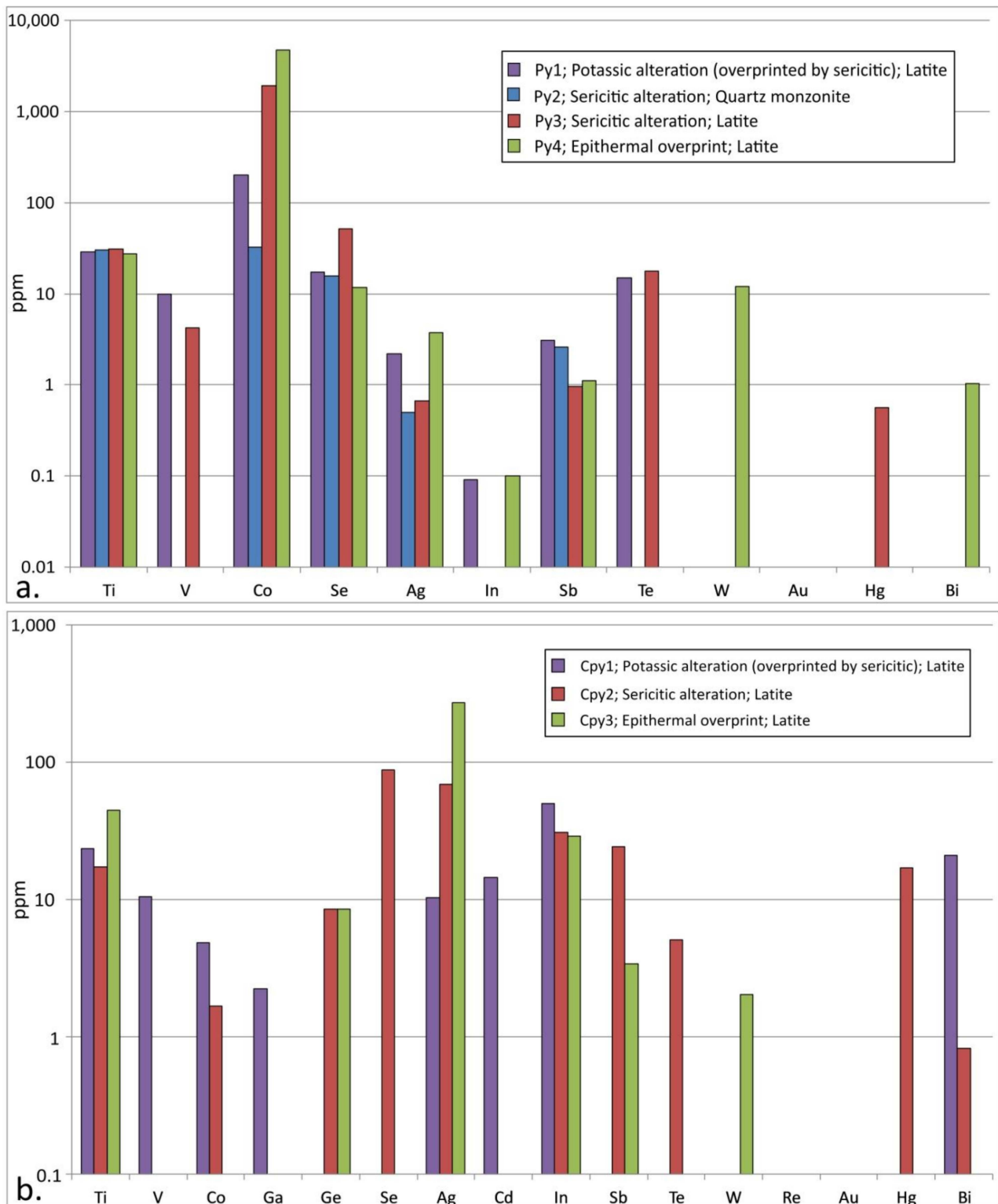


**Figure 9.** Average values of rare metal concentrations of (a) pyrite and (b) chalcopyrite from various mineralization stages. Values are in ppm. Local enrichments related to nano-scale mineral inclusions are excluded.

Several base (As, Cr, Cu, Mn, Mo, Ni, Sn, Zn) and rare metals (Ag, Bi, Co, Hg, In, Sb, Se, Te, Ti, V, W) are incorporated in pyrite (Table 3; Figure 9). Of the four stages of pyrite, Py4 is the most enriched in trace elements, while Py2 is the most depleted one (Figure 9a). Cobalt is the most abundant rare metal, reaching 17,106 ppm in Py4 (Table 3). Silver (< 6.6 ppm in Py4), Ti (<57 ppm in Py1), Se (<200 ppm in Py1), and Sb (<10 ppm in Py3) are present in all pyrite stages (Table 3). Vanadium (<10 ppm) and Te (<41 ppm) were detected in Py1 and Py3, while In (<0.10 ppm) was found in Py1 and Py4. Mercury (<0.7 ppm) occurs in Py3, while W (<27 ppm) and Bi (<1.0 ppm) were found in Py4 (Table 3; Figure 9a).

Trace elements related to nano-scale mineral inclusions include Pb (<2826 ppm in Py1; Supplementary Table S3). Rare metals related to nano-scale mineral inclusions comprise: Ag (<9.4 ppm), Cd (<48 ppm), In (<12 ppm), Au (<5.1 ppm), and Bi (<88 ppm) in Py1; gold (<2.2 ppm), Te (<1237 ppm), and Bi (<1771 ppm) in Py2; Ti (<57 ppm), V (<4 ppm), Co (<342 ppm), Bi (<6.3 ppm), and Th (<0.24 ppm) in Py3; and Ag (<3.7 ppm), Bi (<1.8 ppm), and U (<2.7 ppm) in Py4 (Supplementary Table S3).

Chalcopyrite Cpy1 from the potassic alteration of latite is most enriched with trace elements (Table 4; Figure 9b). Base (As, Cr, Mn, Ni, Pb, Sn, Zn) and rare (Ag, Bi, Co, Cd, Ge, Hg, In, Te, Ti, V, W) metals occur in chalcopyrite (Table 3). Silver (<519 ppm in Cpy2) is the most enriched rare metal and, along with Ti (<45 ppm in Cpy3) and In (<62 ppm in Cpy1), is incorporated in all chalcopyrite stages (Figure 9b). Cobalt (<5.3 ppm) and Bi (<40 ppm) are associated with Cpy1 and Cpy2, while Ge (<12 ppm) and Sb (<48 ppm) are found in Cpy2 and Cpy3 (Figure 9b). Cadmium (<45 ppm), V (<11 ppm), and Ga (<2.3 ppm) are related to Cpy1 (Table 4; Figure 9b). Selenium (<161 ppm), Te (<6.8 ppm), and Hg (<50 ppm) are present in Cpy2, whereas W (<2 ppm) is found in Cpy3 (Figure 9b).

Nano-scale mineral inclusions in chalcopyrite chemistry are associated mainly with Pb and Bi. In Cpy2, Pb and Bi concentrations ascribed to inclusions reach 13,912 ppm and 3111 ppm, respectively (Supplementary Table S3). Additionally, Zn (<5147 ppm), Ag (<9.4 ppm), and Cd (<48 ppm) were detected in Cpy1 (Supplementary Table S3).

#### 4.4.2. Trace Element Compositions of Magnetite and Titanite

Magnetite (Mag1, Mag2) exhibits variations between the analyzed samples, while titanite Ttn1 is characterized by distinctive geochemical patterns. Several rare metals were partitioned between coexisting magnetite and titanite, with titanite being a major host of REE (Table 5; Supplementary Table S3).

Magnetite Mag2 is more enriched with trace elements than Mag1 (Table 5). Various base metals (e.g., Cr, Cu, Mn, Ni, Zn) and a restricted number of rare metals, including Ti, V, Co, Ga, Ge, Se, and W, occur in magnetite (Table 5; Figure 10a). Vanadium (<4176 ppm in Mag1) is the most enriched rare metal, followed by Ti (<2468 ppm in Mag2; Table 5; Figure 11a). Cobalt (<14 ppm) and Ga (<125 ppm) are more enriched in Mag1, whereas Ge (<16 ppm) is more enriched in Mag2. Selenium (<3.3 ppm) and W (<13 ppm) were found in Mag1 and Mag2, respectively (Table 5; Figure 10a).

Rare metals related to the presence of nanoparticles in magnetite (Mag1) include Ti (<3553 ppm), Ag (<1.9 ppm), La (<4.3 ppm), Ce (<7.7 ppm), Bi (<0.92 ppm), and Th (<23 ppm; Supplementary Table S3). Antimony (<2.6 ppm), Ce (<1.2 ppm), Bi (<6.4 ppm), and U (<5.6 ppm; Supplementary Table S3) were detected in Mag2. It should also be mentioned that Cu (<107 ppm) was detected in Mag1, and Pb (<46 ppm in Mag1) was found in Mag2.

**Table 5.** LA-ICP-MS analyses of magnetite and titanite from various mineralization stages. Values are in ppm. For the full dataset, see Supplementary Table S3.

Mineral		Magnetite				Titanite						
Alteration	Potassic-calcic				Potassic (overprinted by sericitic)							
Rock host	Quartz monzonite				Latite							
Mineralization stage	Mag1; M-type veins (n = 7)				Mag2; disseminated (n = 9)				Ttn1; M-type veins (n = 5)			
Element	MIN	MAX	STDEV	AVG	MIN	MAX	STDEV	AVG	MIN	MAX	STDEV	AVG
Al	1062	3161	873	1966	943	4076	1576	2416	4505	5002	209	4741
P	125	364	169	245	b.d.l.	b.d.l.	n.a.	n.a.	365	984	299	617
Ti	1503	1784	154	1607	1074	2468	542	1718	189,900	203,100	4731	195,660
V	3531	4176	219	3763	1831	2832	327	2381	1164	2620	568	2136
Cr	39	282	96	112	63	2043	738	372	b.d.l.	b.d.l.	n.a.	n.a.
Mn	564	734	69	644	467	786	118	660	311	713	156	498
Co	9.8	14	1.6	12	5	13	3.1	8.4	4	4	n.a.	4
Ni	382	814	173	594	11	11	n.a.	11	b.d.l.	b.d.l.	n.a.	n.a.
Cu	36	36	n.a.	36	13	23	5.2	19	47	68	12	57
Zn	37	59	7.9	51	59	137	33	92	38	63	11	50
Ga	78	125	15	109	34	53	6.2	41	12	35	11	18
Ge	2.9	2.9	n.a.	2.9	5.5	16	6.2	3.7	24	40	7	35
As	43	60	12	52	b.d.l.	b.d.l.	n.a.	n.a.	39	146	40	104
Se	3	3.3	n.a.	3.3	b.d.l.	b.d.l.	n.a.	n.a.	74	141	28	102
Nb	n.a.	n.a.	n.a.	n.a.	b.d.l.	b.d.l.	n.a.	n.a.	n.a.	n.a.	n.a.	n.a.
Mo	b.d.l.	b.d.l.	n.a.	n.a.	b.d.l.	b.d.l.	n.a.	n.a.	7.6	11	1.6	8.6
Ag	b.d.l.	b.d.l.	n.a.	n.a.	b.d.l.	b.d.l.	n.a.	n.a.	b.d.l.	b.d.l.	n.a.	n.a.
Cd	b.d.l.	b.d.l.	n.a.	n.a.	b.d.l.	b.d.l.	n.a.	n.a.	b.d.l.	b.d.l.	n.a.	n.a.
In	b.d.l.	b.d.l.	n.a.	n.a.	b.d.l.	b.d.l.	n.a.	n.a.	4.9	10	2.1	7.8
Sn	4.4	13	3.6	8.8	2.9	6	1.3	4.3	1286	2503	496	1988
Sb	b.d.l.	b.d.l.	n.a.	n.a.	b.d.l.	b.d.l.	n.a.	n.a.	11	22	5.4	19
Te	b.d.l.	b.d.l.	n.a.	n.a.	b.d.l.	b.d.l.	n.a.	n.a.	b.d.l.	b.d.l.	n.a.	n.a.
La	b.d.l.	b.d.l.	n.a.	n.a.	b.d.l.	b.d.l.	n.a.	n.a.	576	1369	343	1020
Ce	b.d.l.	b.d.l.	n.a.	n.a.	b.d.l.	b.d.l.	n.a.	n.a.	1813	5535	1487	4047
Nd	n.a.	n.a.	n.a.	n.a.	b.d.l.	b.d.l.	n.a.	n.a.	872	4215	1331	3121
Sm	b.d.l.	b.d.l.	n.a.	n.a.	b.d.l.	b.d.l.	n.a.	n.a.	164	1070	368	792
Gd	b.d.l.	b.d.l.	n.a.	n.a.	b.d.l.	b.d.l.	n.a.	n.a.	131	984	352	736
W	b.d.l.	b.d.l.	n.a.	n.a.	2.7	13	4.8	6.8	11	81	34	31
Re	n.a.	n.a.	n.a.	n.a.	b.d.l.	b.d.l.	n.a.	n.a.	n.a.	n.a.	n.a.	n.a.
Au	b.d.l.	b.d.l.	n.a.	n.a.	b.d.l.	b.d.l.	n.a.	n.a.	b.d.l.	b.d.l.	n.a.	n.a.
Tl	b.d.l.	b.d.l.	n.a.	n.a.	b.d.l.	b.d.l.	n.a.	n.a.	b.d.l.	b.d.l.	n.a.	n.a.
Pb	b.d.l.	b.d.l.	n.a.	n.a.	b.d.l.	b.d.l.	n.a.	n.a.	b.d.l.	b.d.l.	n.a.	n.a.
Bi	b.d.l.	b.d.l.	n.a.	n.a.	b.d.l.	b.d.l.	n.a.	n.a.	b.d.l.	b.d.l.	n.a.	n.a.
Th	b.d.l.	b.d.l.	n.a.	n.a.	b.d.l.	b.d.l.	n.a.	n.a.	32	309	103	206
U	n.a.	n.a.	n.a.	n.a.	b.d.l.	b.d.l.	n.a.	n.a.	n.a.	n.a.	n.a.	n.a.

Abbreviations: AVG = average value; b.d.l. = below detection limit; MIN = minimum value; MAX = maximum value; n = number of analyses; n.a. = not analyzed; STDEV = standard deviation.

Titanite (Ttn1) hosts base (As, Cu, Mn, Sn) and rare (e.g., V, Th, Se, W) metals and is enriched with REE (Table 5; Figure 10b). Rare metals comprise V (<2620 ppm), Th (<309 ppm), Se (<141 ppm), W (<81 ppm), Ge (<40 ppm), Ga (<35 ppm), Sb (<22 ppm), In (<10 ppm), and Co (<4 ppm; Figure 10b). Rare-earth elements in Ttn2 include Ce (<5535 ppm), which is the most enriched trace element, followed by La (1369 ppm), Nd (421 ppm), Sm (1070 ppm), and Gd (986 ppm; Table 5; Figure 10b). Enrichments of rare metals related to nano-scale mineral inclusions were not detected in titanite.

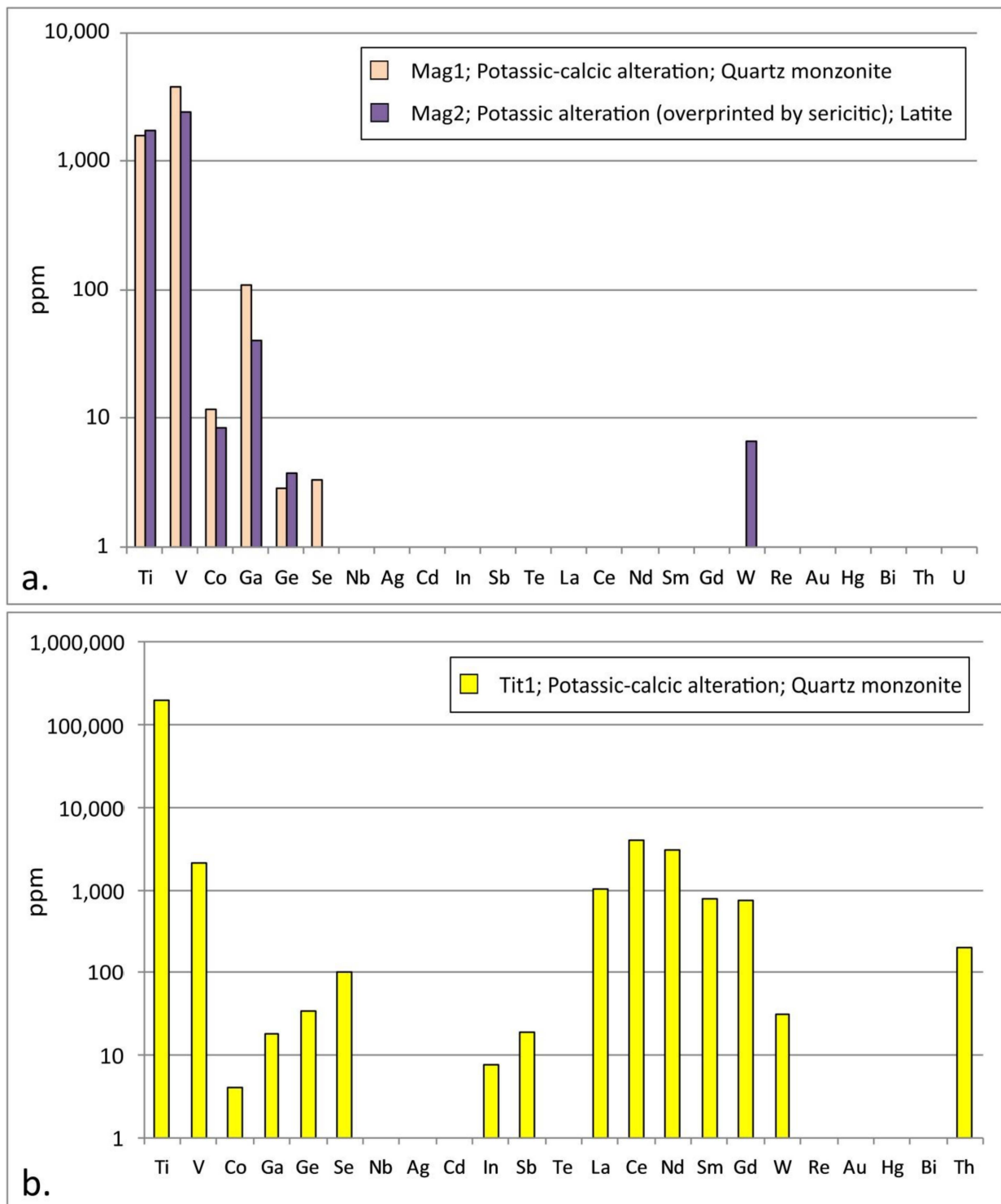


**Figure 10.** Average values of rare metal concentrations of (a) magnetite and of (b) titanite from various mineralization stages. Values are in ppm. Local enrichments related to nano-scale mineral inclusions are excluded.

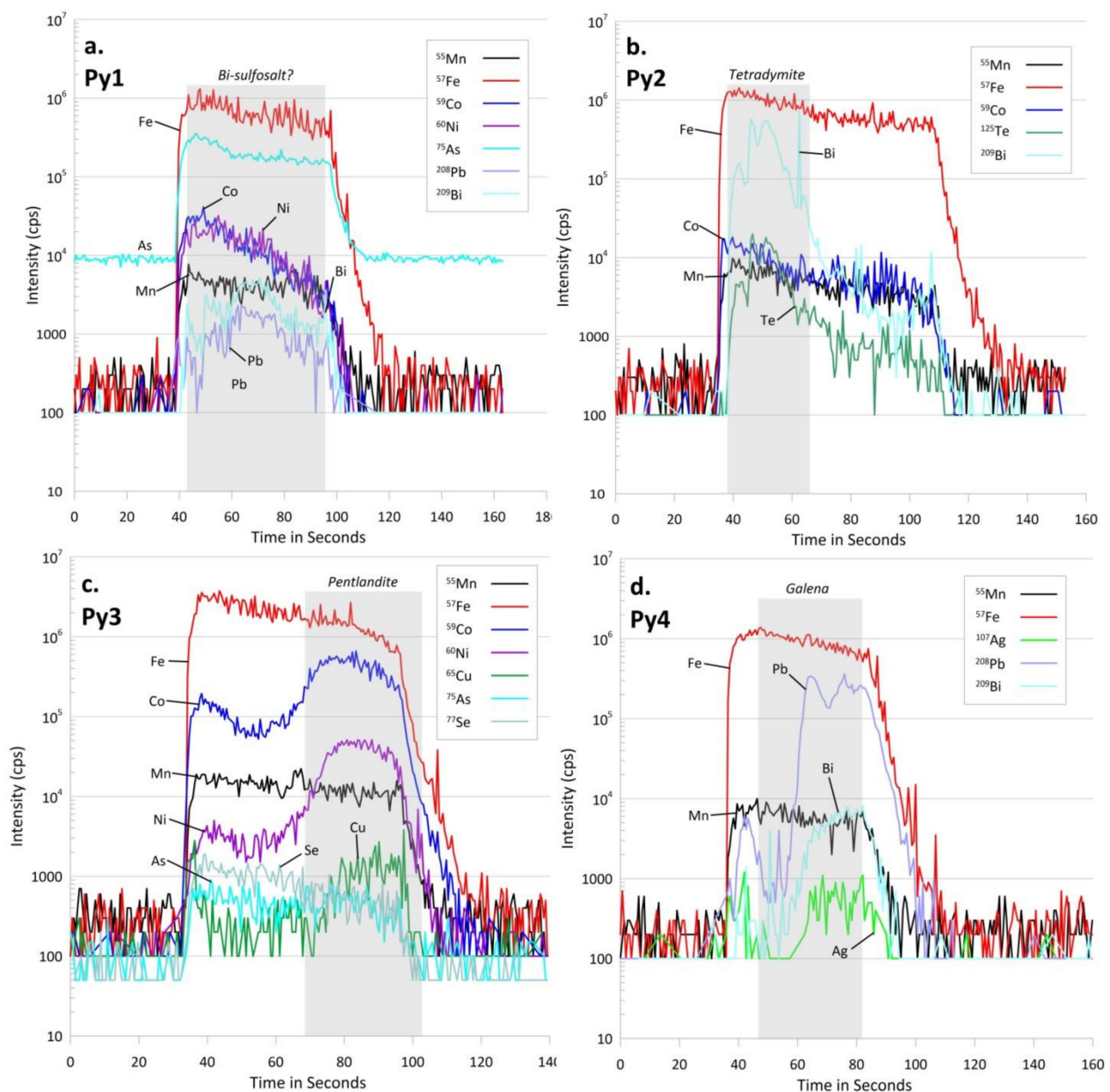


**Figure 11.** Selected time-resolved laser ablation ICP-MS depth profiles of pyrite (a–d) from the different groups and their associated inclusions (highlighted in gray). Manganese, Co, Ni, and As, where present, exhibit similar distribution patterns to Fe, unless stated otherwise: (a) in Py1, the distribution patterns of Bi and Pb could be related to nano-scale inclusions of Bi-sulfosalts; (b) in Py2, the spiky patterns for Bi and Te could suggest the presence of nano-scale inclusions of tetradymite; (c) in Py3, the similarly curved distribution patterns could be associated with the presence of pentlandite inclusions; (d) in Py4, the spiky patterns of Pb, Bi, and Ag could suggest the occurrence of galena inclusions.

#### 4.4.3. Statistical Analysis of Trace Element Concentrations

In order to further investigate the chemistry of pyrite, chalcopyrite, magnetite, and titanite, and the geochemical association of the detected and measured rare metals, Pearson product-moment correlation coefficients and associated *p*-values were calculated for the LA-ICP-MS analyses. Heat maps of the Pearson correlation coefficient matrix for pyrite, chalcopyrite, magnetite, and titanite are given in Supplementary Table S4. Based on data reduction and ablation patterns, trace element concentrations related to nano-scale mineral

inclusions, or nanoparticles in the case of magnetite, were excluded before the statistical analyses.

Pearson product-moment correlation coefficients for pyrite are described by significant positive correlations ( $p < 0.01$ ; values  $\geq 0.883$ ) defined for the elemental pairs Ag–Sb, Co–In, Co–V, Se–V, and Se–W (Supplementary Table S4). Significant negative correlations ( $p < 0.01$ ; values  $\geq -1.0$ ) occur for the elemental pairs Hg–Sb and In–Se. Significant positive correlations ( $p < 0.01$ ; values  $\geq 0.797$ ) are noted for the elemental pairs Ag–Se, Co–Se, Co–Te, Hg–Ti, and Sb–Se in chalcopyrite. Positive correlations ( $p < 0.05$ ; values  $\geq 0.622$ ) occur between Ag and Hg, as well as for the following pairs Ag–Ti, Bi–Co, Co–Hg, and Hg–Se. Significant negative correlations ( $p < 0.01$ ; values  $\geq -0.59$ ) include the pairs Ag–In and Ge–Se.

Magnetite is characterized by significant positive correlations for the pair Ga–V ( $p < 0.01$ ; value: 0.844), and by positive correlations for Co–V, and V–W ( $p < 0.05$ ; values: 0.677, 0.956), while significant negative correlations were not detected for any elemental pairs (Supplementary Table S4). Strong positive correlation coefficients ( $p < 0.01$ ; values  $\geq 0.960$ ) occur for the elemental pairs Ce–La, Gd–Nd, Gd–Sm, Nd–Sm, Ge–Sb, Nd–V, and Sm–V in titanite (Supplementary Table S4), while smaller positive correlations ( $p < 0.05$ ; values  $\geq 0.884$ ) occur between Ce and Ge, Nd, Th, and V, between Ge and La, Nd, Th, and V, and for the pairs Ga–Th, Gd–V, Nd–Th, Sm–Th, and Th–U (Supplementary Table S4). Significant negative correlations ( $p < 0.01$ ; values  $\geq -0.996$ ) occur for the pairs Ge–W and Sb–W.

## 5. Discussion

### 5.1. Hydrothermal Alterations, Mineralization Stages, and Bulk Geochemistry

Porphyry Cu–Au–Mo deposits are potential exploration and exploitation targets for rare metals, as they exhibit enrichments of PGE, Re, Te, Co, Bi, and U [9,10]. The polymetallic assemblages found in the periphery of porphyry systems related to skarn, replacement, vein, and intermediate sulfidation epithermal mineralization types are enriched with Mn, Ge, Ga, In, Bi, Sb, As, W, and Te [9–11,27]. In addition, low- to high-sulfidation mineralization associated with epithermal overprinting of porphyry systems may include Te, Bi, As, Sb, V, and F [9–11,27].

At the Vathi deposit, the hydrothermal alteration, the porphyry and epithermal-related mineralization stages, the bulk geochemistry, and the mineral chemistry reveal specific mineralogical and geochemical relations to various rare metals (e.g., Ag, Au, Bi, Co, Se, Te, and W; Table 2). The REE distribution and relative REE enrichment at Vathi are ascribed to monazite and titanite, and possibly to other rock-forming and alteration minerals (e.g., feldspar [53]). The relatively fresh and unoxidized quartz monzonite (Vath 41) includes the highest concentrations of Ce, Gd, La, Nd, and Sm, which are significantly correlated with each other (Figure 5; Supplementary Table S4). The comparison between the new and the previously published bulk geochemical analysis at Vathi emphasizes the effect of supergene processes on the enrichment of the rare metals (Table 2; Supplementary Table S1; [53]).

The metallic and alteration assemblages related to potassic-calcic alteration and the complete absence of sulfide minerals suggest the highly oxidized nature of the initial fluids, as well as the high solubility of Fe and  $\text{FeCl}_2$  [30] (Table 1). This type of alteration exhibits the lowest enrichment of rare metals (Table 2; Figure 5). Tungsten, Ce, Th, Nd, and La are the most enriched rare metals at concentrations  $< 75$  ppm and are significantly correlated with each other (Supplementary Table S4). In Greece, M-type veins have been previously described from the Pagoni-Rachi, the Maronia, and the Stypsi porphyry deposits [33,49,66]. The M-type veins at Vathi are different in terms of the contained metallic and alteration assemblages and are not associated with the introduction of any hypogene mineralization, as is the case at Pagoni-Rachi [33,49,66].

The potassic alteration that was overprinted by sericitic alteration is associated with A-type veins in the quartz monzonite and with disseminations in the latite at Vathi (Table 1; Figures 4b, 6a and 7a). The formation of the A-type veins was a restricted event in terms of

size and occurrence. According to Stergiou et al. [53], the formation of the A-type veins is related to boiling hydrothermal fluids at temperatures  $> 390$  °C (646 bars;  $< 2.6$  km in depth). The A-type veins are related to a restricted introduction of gold in the Vathi magmatic-hydrothermal system (Table 1; Figure 6a).

The sericitic alteration is characterized by D-type veins and disseminations in both the quartz monzonite and the latite (Table 1; Figure 3d,e). The sericitic alteration and the associated metallic and alteration assemblages formed at temperatures ranging between 311 and 392 °C, from a moderately saline (8.4–11.2 wt.% NaCl equiv.) fluid [53]. Tetradymite and native gold are spatially related to the mineralization of the quartz monzonite (Figures 6c and 7c,d). Bismuth tellurides, Bi-sulfosalts, and Au-Ag-tellurides have been previously reported from calc-alkaline to alkaline porphyry deposits in northern Greece [67]. Tetradymite associated with sericitic alteration was recognized from the Koryfes porphyry deposit, whereas in the Papadokoryfi and Pagoni-Rachi porphyry deposits, tetradymite is found in the porphyry–epithermal transition environment [38]. The occurrence of pyrrhotite, pentlandite, wittichenite, fletcherite, and cuprobismutite found in the latite at Vathi is uncommon or is rarely described for the sericitic alteration of the porphyry deposits found elsewhere in Greece [38]. At Vathi, pyrrhotite and pentlandite are found as inclusions along with chalcopyrite in pyrite disseminations and aggregates, while fletcherite, wittichenite, and cuprobismutite occur as inclusions in chalcopyrite aggregates (Figures 6d and 7e). These textural characteristics suggest a Ni, Co, Bi, and Ag enrichment and shifts in  $fO_2/fS_2$  conditions for the mineralizing fluids of this stage. Shifts in sulfur fugacity caused by the interaction between the late-mineralizing fluids and carbonaceous wall rocks have been previously suggested for Vathi [53].

Bulk geochemical analysis showed that rare metals are enriched in the sericitic alteration (Table 2; Figure 5). Gold (0.8 ppm), Te (1.5 ppm), and Co (450 ppm) exhibit their highest enrichment in this alteration, while Se (2.8 ppm), Bi (3.4 ppm), and Ag (0.9 ppm) are also enriched (Table 2). In addition, Pearson's correlation coefficients suggested significant correlations for the pairs Ag–Au, Au–Te, and Au–Se (Supplementary Table S4). These results verify the association among tetradymite and native gold. According to Voudouris et al. [38], the porphyry- and epithermal-style gold mineralization in Greece is classified as follows for deposits where: (a) native gold and Au–Ag–tellurides are associated with Bi-sulfosalts and oxidized-type Bi-sulfotellurides; (b) native gold is related to Bi-sulfosalts; and (c) native gold and Au–Ag–tellurides are only present. Using this classification scheme, Vathi belongs to the first category.

The epithermal overprint occurs in the sericitic alteration of latite and is associated with E-type veins and cataclasite (Figures 2 and 3f,g; [53]). The epithermal stage, according to Stergiou et al. [53], developed between 205 and 259 °C, from a slightly saline (1.4–2.9 wt.% NaCl equiv.) fluid. Epithermal (E-type) veins related to the porphyry–epithermal transition environment have been previously described in Greece (e.g., Pagoni-Rach, Stypsi, Maronia, Skouries) [33,38]. At Vathi, the E-type veins host base metal sulfides only (Table 1).

## 5.2. Mineral Chemistry of Pyrite and Chalcopyrite and Nano-Scale Inclusions

Pyrite and chalcopyrite can be associated with significant amounts or rare metals incorporated as nano-scale mineral inclusions or as nanoparticles [13,14,18–22,24]. These inclusions can be formed due to exsolution from the pyrite or chalcopyrite matrix, as well as through precipitation from the hydrothermal fluid into the growing mineral [14,24]. In pyrite, nano-scale mineral inclusions are mostly related to electrum, galena, tellurides, and cinnabar, whereas in chalcopyrite, sphalerite and micro-inclusions related to Zn-, As-, Pb-, and Au-bearing phases are reported [14,24]. The interpretation of the scanning electron microscopy and LA-ICP-MS analyses for pyrite and chalcopyrite at Vathi suggests that specific minerals occur as nano-inclusions.

All the pyrite stages (Py1–4) at Vathi are enriched with Ag, Co, Sb, Se, and Ti (Table 3; Figure 9a). In contrast, Hg, Te, and V are elevated in Py1, Py2, and Py3, whereas Bi and W

are present in Py4 of the late-stage epithermal overprint. Indium is associated with Py1 in the potassic alteration and the epithermal overprint (Py4) (Figure 9a). It is suggested here that based on the ablation patterns, Co and Se are incorporated in pyrite as stoichiometric substitutions. Cobalt and Se are considered common stoichiometric substitutions for Fe and S, respectively [13]. In addition, restricted amounts of Ag, Bi, Hg, In, Sb, Ti, V, and W could be accommodated in the pyrite structure as solid solutions (Table 2; [13,24]). Based on the concentrations of some elements and the laser ablation patterns, several enrichments in trace elements of pyrite are attributed to nano-scale mineral inclusions (Supplementary Table S3; Figure 11). The rare metals related to inclusions comprise: Ag, Au, Bi, Cd, and In in Py1; Au, Bi, and Te in Py2; Bi, Co, Th, Ti, and V in Py3; and Ag, Bi, and U in Py4. Lead enrichment could be attributed to nano-scale inclusions of galena in Py2, Py3, and Py4. These trace elements could be associated with Bi-sulfosalts for Py1, with tetradymite for Py2, with pentlandite for Py3, and with galena for Py4 (Figure 11a–d). Furthermore, based on the concentrations of Au and Cu, nano-inclusions of native gold are accommodated in Py1 and Py2, and chalcopyrite is hosted in Py2. Chalcopyrite Cpy1 (potassic alteration; latite) and Cpy2 (sericitic alteration; latite), as well as chalcopyrite Cpy3 (E-type veins), contain enrichments of Ag, In, and Ti (Table 4; Figure 9b). Cadmium, Ga, and V are related to Cpy1, and Hg, Se, and Te were found only in Cpy2, while Bi and Co are associated with Cpy1 and Cpy2 (Figure 9b). Germanium and Sb were found in Cpy2 and Cpy3, while W was measured only in Cpy3 from the E-type veins. Based on the ablation patterns Ag, Bi, Cd, Co, Ga, Ge, Hg, In, Sb, Se, Te, Ti, V, and W are accommodated in chalcopyrite in solid solutions.

Concentrations of trace elements ascribed to nano-scale mineral inclusions in chalcopyrite include mainly Bi and Pb, while Ag, Cd, and Zn were attributed to inclusions in Cpy1 (Supplementary Table S3; Figure 12a,b). Zinc and Cd enrichments (Cpy1) are likely related to the presence of sphalerite nano-scale inclusions, while Bi and Pb (Cpy1, Cpy2), and Ag (Cpy1) are probably due the presence of Bi-sulfosalts (Figure 12a,b). Chalcopyrite Cpy3 exhibits minor Pb enrichments, probably due to galena inclusions. It is noted that the presence of Bi-sulfosalts in Cpy2 is also supported by the presence of wittichenite and cuprobismutite (Figure 7e).

### 5.3. Mineral Chemistry of Magnetite and Titanite and Nano-Scale Inclusions

Aluminum, Co, Cr, Ga, Mg, Mn, Ni, Ti, V, and Zn typically substitute primary cations in magnetite participating in a crystal lattice [15,16]. Additionally, Al, Ca, Mg, Na, Si, Ti, and V can be found as nanoparticles in growth or sector zones in magnetite [25]. Titanite is considered a major host of Zr, Hf, Nb, Ta, Ti, Sr, V, Sc, and REE [31]. These elements are found structurally bound in titanite [17,31,32]. The combined interpretation of the scanning electron microscopy and LA-ICP-MS analyses for magnetite and titanite at Vathi supports these conclusions.

Magnetite (Mag1) from the M-type veins related to the potassic-calcic alteration in the quartz monzonite and magnetite (Mag2) from the potassic alteration in latite are associated with rare metals including Co, Ga, Ge, Ti, and V, while W occurs in Mag2. These elements are likely incorporated as stoichiometric substitutions (Table 5; Figure 10a). Trace elements associated with nanoparticles include Ag, Bi, Ce, Cu, La, Pb, Th, and Ti for Mag1, and Bi, Ce, Sb, and U for Mag2 (Supplementary Table S3). Ablation patterns and SEM-EDS analysis support the concept that titanite is hosted as inclusions of various sizes in Mag1 (Figures 8b and 12c). The presence of Pb and S in Mag2 could be related to minor nano-scale galena inclusions.

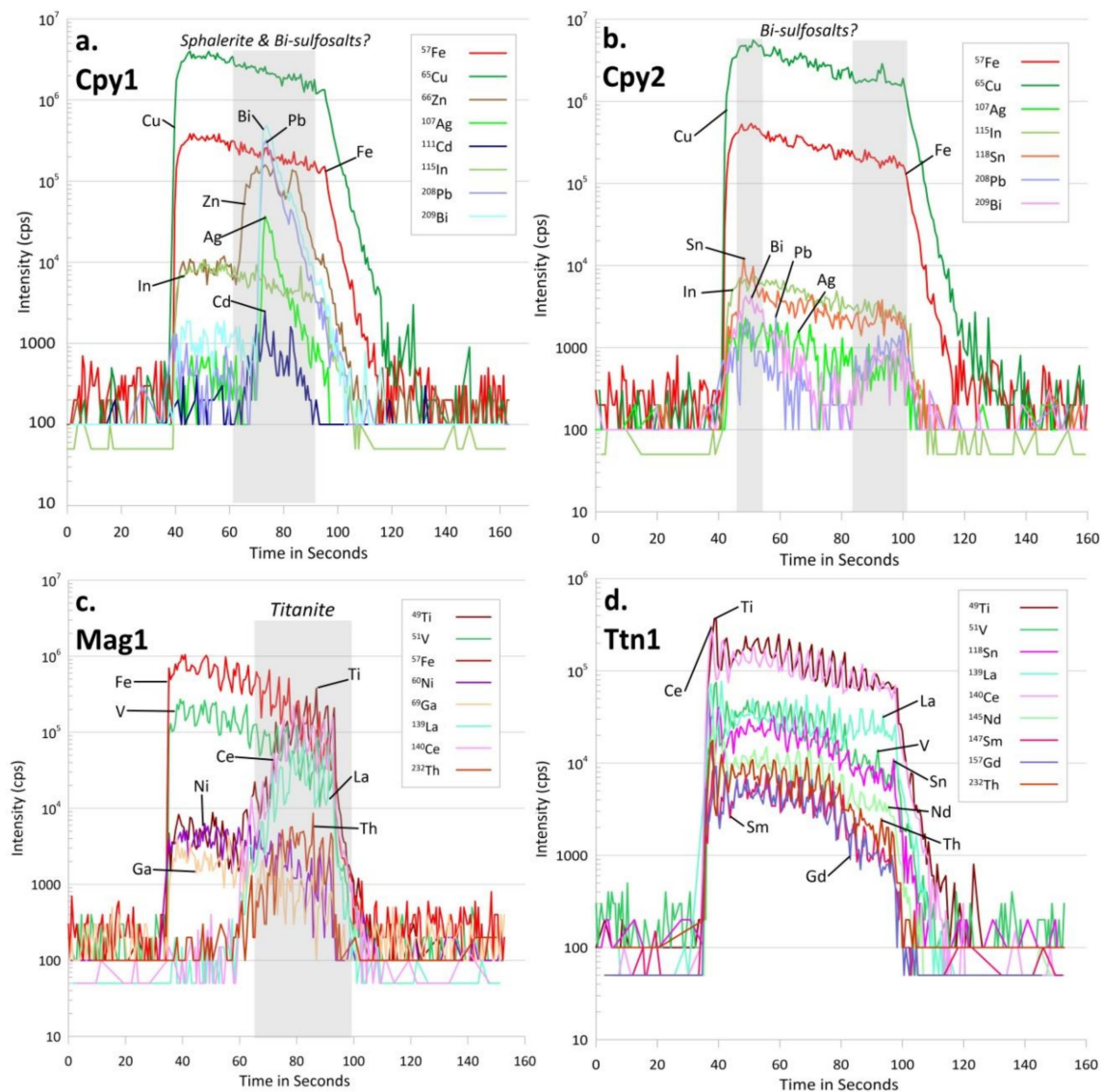


**Figure 12.** Selected time-resolved laser ablation ICP-MS depth profiles of chalcopyrite (a,b), magnetite (c), and titanite (d) and their associated inclusions (highlighted in gray). Iron, In, Ag, and Sn, where present, exhibit similar distribution patterns to Cu, in Cpy1 and Cpy2: (a) in Cpy1, the spiky patterns of Zn and Cd suggest the presence of sphalerite as nano-scale inclusions, while the more spiky patterns for Bi, Pb, and Ag could be related to nano-scale inclusions of silver-rich Bi-sulfosalts; (b) in Cpy2, the curved patterns of Bi and Pb could be associated with Bi-sulfosalts found as nano-scale inclusions; (c) in Mag1, vanadium, Ni, and Ga follow similar distribution patterns to iron, while the spiky patterns indicate a titanite inclusion in magnetite; in the titanite inclusion, La, Ce, and thorium follow the distribution patterns of Ti; (d) in Ttn1, vanadium, Sn, La, Ce, Nd, Sm, Gd, and Th show similar distribution patterns. Mineral inclusions were not detected in titanite (Ttn1).

Titanite (Ttn1) from the potassic-calcic alteration associated with quartz monzonite is enriched with Ce, Gd, La, Nd, and Sm and hosts several rare metals including Co, Ga, Ge, In, Sb, Se, Th, and V (Table 5). These elements constitute stoichiometric substitutions since nano-scale mineral inclusions were not detected (Figure 12d).

## 6. Conclusions

The Vathi porphyry Cu–Au±Mo deposit shows enrichments of rare and critical metals including Ag, Au, Bi, Cd, Co, Ga, Ge, Hg, In, Nb, Sb, Se, Te, Th, Ti, V, W, and REE (Ce, Gd, La, Nd, and Sm). Native gold occurs in A-type veins crosscutting the potassic

alteration that is overprinted by sericitic alteration in quartz monzonite, and in D-type veins found in both the quartz monzonite and the latite. Native gold is more widespread in the sericitic alteration, where it occurs with tetradymite in the quartz monzonite, and with wittichenite and cuprobismutite in the latite.

Samples from the potassic and sericitic alterations show significant enrichments of rare metals including Ag, Au, Bi, Co, Se, Te, and W. Rare-earth element enrichment is not related to the porphyry and epithermal mineralizing events but is attributed mostly to rock-forming and supergene processes. Pyrite at Vathi is enriched with Ag, Co, Sb, Se, and Ti, while moderate and weak enrichments have been detected for Bi, Hg, Te, V, and W, and for In, respectively. Chalcopyrite contains elevated concentrations of Ag, In, and Ti and is moderately enriched with Bi, Cd, Co, Ga, Hg, Se, Te, V, and W, and weakly enriched with Nb. High concentrations of Co, Ga, Ge, Ti, and V and low concentrations of Se and W occur in magnetite. Titanite is a major host of REE including Ce, Gd, La, Nd, and Sm, as well as being a major host of Co, Ga, Ge, In, Sb, Se, Th, and W. Nano-scale mineral inclusions are hosted in pyrite and chalcopyrite, while enrichments of Ag, Bi, Ce, Cu, La, Pb, Th, and U are related to nanoparticles partitioning into magnetite. Nano-scale mineral inclusions are likely related to the presence of Bi-sulfosalts and native gold in pyrite in the potassically altered latite. In addition, chalcopyrite, tetradymite, and native gold in pyrite from the sericitic alteration in quartz monzonite, pentlandite in pyrite from the sericitic alteration in latite, and galena in pyrite in the epithermal overprint are also likely nano-inclusions. Nano-scale inclusions occur as sphalerite and Bi-sulfosalts in chalcopyrite from the potassic alteration in latite, and as Bi-sulfosalts in chalcopyrite from the sericitic alteration of the latite. Nano-scale inclusions of galena are accommodated in chalcopyrite from E-type veins. Inclusions of wittichenite, tetradymite, and cuprobismutite reflect enrichments of Te and Bi in the mineralizing fluids associated with sericitic alteration. Magnetite from the potassic-calcic alteration of the quartz monzonite hosts titanite inclusions, while minor amounts of nano-scale inclusions of galena likely occur in magnetite from the potassic alteration in latite. Titanite from the potassic-calcic alteration of the quartz monzonite contains no nano-inclusions.

**Supplementary Materials:** The following are available online at <https://www.mdpi.com/article/10.3390/min11060630/s1>, Table S1: Bulk geochemistry, Table S2: SEM-EDS data, Table S3: LA-ICP-MS data, Table S4: Pearson's correlation coefficient table.

**Author Contributions:** Conceptualization, C.L.S., V.M.; methodology, V.M., L.P., I.P., E.S., D.D.; formal analysis, L.P., I.P., E.S., D.D.; data curation, C.L.S., E.S., D.D., K.G.; writing—original draft preparation, C.L.S.; writing—review and editing, C.L.S., V.M., P.V., L.P., I.P., D.D.; E.S., K.G., P.G.S.; supervision, V.M., P.V., L.P.; funding acquisition, C.L.S. All authors have read and agreed to the published version of the manuscript.

**Funding:** The ore microscopy and rock geochemistry investigation was funded by a research grant from the Society of Economic Geologists Canada Foundation (SEGCF) Fund. C.L.S received a scholarship co-financed by Greece and the European Union (European Social Fund—ESF) through the operational program «Human Resources Development, Education and Lifelong Learning» in the context of the project “Strengthening Human Resources Research Potential via Doctorate Research” (MIS-5000432), implemented by the State Scholarships Foundation (IKY).

**Data Availability Statement:** The data presented in this study are available in the Supplementary Materials in Tables S1–S4.

**Acknowledgments:** The authors would like to acknowledge the Geological Institute of the Bulgarian Academy of Sciences for facilitating the LA-ICP-MS analysis. Two anonymous reviewers are kindly thanked for providing comments that highly improved the manuscript.

**Conflicts of Interest:** The authors declare no conflict of interest. The funders had no role in the design of the study; in the collection, analyses, or interpretation of data; in the writing of the manuscript, or in the decision to publish the results.

## References

1. Verplanck, P.L.; Hitzman, M.W. Introduction: Rare Earth and Critical Elements in Ore Deposits. In *Rare Earth and Critical Elements in Ore Deposits*; Society of Economic Geologists Inc.: Littleton, CO, USA, 2016; pp. 1–4.
2. Ayres, R.U.; Peiro, L.T. Material efficiency: Rare and critical metals. *Philos. Trans. R. Soc. A* **2013**, *371*, 20110563. [[CrossRef](#)] [[PubMed](#)]
3. Bertrand, G.; Cassard, D.; Arvanitidis, N.; Stanley, G. Map of critical raw material deposits in Europe. *Energy Procedia* **2016**, *97*, 44–50. [[CrossRef](#)]
4. Watari, T.; Nansai, K.; Nakajima, K. Review of critical metal dynamics to 2050 for 48 elements. *Resour. Conserv. Recycl.* **2020**, *155*, 104669. [[CrossRef](#)]
5. European Commission. *Critical Raw Materials Resilience: Charting a Path towards Greater Security and Sustainability*; European Commission: Brussels, Belgium, 2020; p. 24.
6. Verplanck, P.L.; Mariano, A.N.; Mariano, A., Jr. Rare earth element ore geology of carbonatites. In *Rare Earth and Critical Elements in Ore Deposits*; Verplanck, P.L., Hitzman, M.W., Eds.; Society of Economic Geologists Inc.: Littleton, CO, USA, 2016; pp. 5–32.
7. Dostal, J. Rare metal deposits associated with alkaline/peralkaline igneous rocks. In *Rare Earth and Critical Elements in Ore Deposits*; Verplanck, P.L., Hitzman, M.W., Eds.; Society of Economic Geologists Inc.: Littleton, CO, USA, 2016; pp. 33–54.
8. Sengupta, D.; Van Gosen, B.S. Placer-type rare earth element deposits. In *Rare Earth and Critical Elements in Ore Deposits*; Verplanck, P.L., Hitzman, M.W., Eds.; Society of Economic Geologists Inc.: Littleton, CO, USA, 2016; pp. 81–100.
9. John, D.A.; Taylor, R.D. By-products of porphyry copper and molybdenum deposits. In *Rare Earth and Critical Elements in Ore Deposits*; Verplanck, P.L., Hitzman, M.W., Eds.; Society of Economic Geologists Inc.: Littleton, CO, USA, 2016; pp. 137–164.
10. Kelley, K.D.; Spry, P.G. Critical elements in alkaline igneous rock-related epithermal gold deposits. In *Rare Earth and Critical Elements in Ore Deposits*; Verplanck, P.L., Hitzman, M.W., Eds.; Society of Economic Geologists Inc.: Littleton, CO, USA, 2016; pp. 195–216.
11. Goldfarb, R.J.; Hofstra, A.H.; Simmons, S.F. Critical elements in Carlin, epithermal, and orogenic gold deposits. In *Rare Earth and Critical Elements in Ore Deposits*; Verplanck, P.L., Hitzman, M.W., Eds.; Society of Economic Geologists Inc.: Littleton, CO, USA, 2016; pp. 217–244.
12. Velásquez, G.; Carrizo, D.; Salvi, S.; Vela, I.; Pablo, M.; Pérez, A. Tracking cobalt, REE and gold from a porphyry-type deposit by LA-ICP-MS: A geological approach towards metal-selective mining in tailings. *Minerals* **2020**, *10*, 109. [[CrossRef](#)]
13. Abraitis, P.K.; Patrick, R.A.D.; Vaughan, D.J. Variations in the compositional, textural and electrical properties of natural pyrite: A review. *Int. J. Miner. Process.* **2004**, *74*, 41–59. [[CrossRef](#)]
14. George, L.L.; Cook, N.J.; Crowe, B.B.; Ciobanu, C.L. Trace elements in hydrothermal chalcopyrite. *Mineral. Mag.* **2018**, *82*, 59–88. [[CrossRef](#)]
15. Nadoll, P.; Mauk, J.L.; Leveille, R.A.; Koenig, A.E. Geochemistry of magnetite from porphyry Cu and skarn deposits in the southwestern United States. *Miner. Depos.* **2014**, *50*, 493–515. [[CrossRef](#)]
16. Huang, X.W.; Sappin, A.A.; Boutroy, É.; Beaudoin, G.; Makvandi, S. Trace element composition of igneous and hydrothermal magnetite from porphyry deposits: Relationship to deposit subtypes and magmatic affinity. *Econ. Geol.* **2019**, *114*, 917–952. [[CrossRef](#)]
17. Xu, L.; Bi, X.; Hu, R.; Tang, Y.; Wang, X.; Xu, Y. LA-ICP-MS mineral chemistry of titanite and the geological implications for exploration of porphyry Cu deposits in the Jinshajiang—Red River alkaline igneous belt, SW China. *Miner. Petrol.* **2015**, *109*, 181–200. [[CrossRef](#)]
18. Dmitrijeva, M.; Cook, N.J.; Ehrig, K.; Ciobanu, C.L.; Metcalfe, A.V.; Kamenetsky, M.; Kamenetsky, V.S.; Gilbert, S. Multivariate statistical analysis of trace elements in pyrite: Prediction, bias and artefacts in defining mineral signatures. *Minerals* **2020**, *10*, 61. [[CrossRef](#)]
19. Keith, M.; Smith, D.J.; Doyle, K.; Holwell, D.A.; Jenkin, G.R.T.; Barry, T.L.; Becker, J.; Rampe, J. Pyrite chemistry: A new window into Au-Te ore-forming processes in alkaline epithermal districts, Cripple Creek, Colorado. *Geochim. Cosmochim. Acta* **2020**, *274*, 172–191. [[CrossRef](#)]
20. Reich, M.; Román, N.; Barra, F.; Morata, D. Silver-rich chalcopyrite from the active Cerro Pabellón geothermal system, northern Chile. *Minerals* **2020**, *10*, 113. [[CrossRef](#)]
21. Marfin, A.E.; Ivanov, A.V.; Abramova, V.D.; Anziferova, T.N.; Radomskaya, T.A.; Yakich, T.Y.; Bestemianova, K.V. A trace element classification tree for chalcopyrite from Oktyabrsk deposit, Norilsk–Talnakh Ore District, Russia: LA-ICPMS Study. *Minerals* **2020**, *10*, 716. [[CrossRef](#)]
22. Mavrogenatos, C.; Voudouris, P.; Zaccarini, F.; Klemme, S.; Berndt, J.; Tarantola, A.; Melfos, V.; Spry, P.G. Multi-stage introduction of precious and critical metals in pyrite: A case study from the Konos Hill and Pagoni Rachi porphyry/epithermal prospects, NE Greece. *Minerals* **2020**, *10*, 784. [[CrossRef](#)]
23. Mavrogenatos, C.; Voudouris, P.; Berndt, J.; Klemme, S.; Zaccarini, F.; Spry, P.G.; Melfos, V.; Tarantola, A.; Keith, M.; Klemd, R.; et al. Trace elements in magnetite from the Pagoni Rachi porphyry prospect, NE Greece: Implications for ore genesis and exploration. *Minerals* **2019**, *9*, 725. [[CrossRef](#)]
24. Deditius, A.P.; Utsunomiya, S.; Reich, M.; Kesler, S.E.; Ewing, R.C.; Hough, R.; Walshe, J. Trace metal nanoparticles in pyrite. *Ore Geol. Rev.* **2011**, *42*, 32–46. [[CrossRef](#)]

25. Deditius, A.P.; Reich, M.; Simon, A.C.; Suvorova, A.; Knipping, J.; Roberts, M.P.; Rubanov, S.; Dodd, A.; Saunders, M. Nanogeochemistry of hydrothermal magnetite. *Contrib. Mineral. Petrol.* **2018**, *173*, 1–20. [[CrossRef](#)]
26. Dimitrova, D.; Mladenova, V.; Hecht, L. Efflorescent sulfate crystallization on fractured and polished colloform pyrite surfaces: A migration pathway of trace elements. *Minerals* **2020**, *10*, 12. [[CrossRef](#)]
27. Sillitoe, R.H. Porphyry copper systems. *Econ. Geol.* **2010**, *105*, 3–41. [[CrossRef](#)]
28. Pudack, C.; Halter, W.E.; Heinrich, C.A.; Pettke, T. Evolution of magmatic vapor to gold-rich epithermal liquid: The porphyry to epithermal transition at Nevados de Famatina, northwest Argentina. *Econ. Geol.* **2009**, *104*, 449–477. [[CrossRef](#)]
29. Canil, D.; Grondahl, C.; Lacourse, T.; Pisiak, L.K. Trace elements in magnetite from porphyry Cu–Mo–Au deposits in British Columbia, Canada. *Ore Geol. Rev.* **2016**, *72*, 1116–1128. [[CrossRef](#)]
30. Arancibia, O.N.; Clark, A.H. Early magnetite-amphibole-plagioclase alteration mineralization in the Island Copper porphyry copper-gold-molybdenum deposit, British Columbia. *Econ. Geol.* **1996**, *91*, 402–438. [[CrossRef](#)]
31. Tiepolo, M.; Oberti, R.; Vannucci, R. Trace-element incorporation in titanite: Constraints from experimentally determined solid/liquid partition coefficients. *Chem. Geol.* **2002**, *191*, 105–119. [[CrossRef](#)]
32. Cao, M.J.; Qin, K.Z.; Li, Q.M.; Evans, N.J.; Jin, L.Y. In situ LA-(MC)-ICP-MS trace element and Nd isotopic compositions and genesis of polygenetic titanite from the Baogutu reduced porphyry Cu deposit, Western Junggar, NW China. *Ore Geol. Rev.* **2015**, *65*, 940–954. [[CrossRef](#)]
33. Melfos, V.; Voudouris, P.; Melfou, M.; Sánchez, M.G.; Papadopoulou, L.; Filippidis, A.; Spry, P.G.; Schaarschmidt, A.; Klemm, R.; Haase, K.M.; et al. Mineralogical constraints on the potassic and sodic-calcic hydrothermal alteration and vein-type mineralization of the Maronia porphyry Cu–Mo ± Re ± Au deposit in NE Greece. *Minerals* **2020**, *10*, 182. [[CrossRef](#)]
34. Ross, J.; Voudouris, P.; Melfos, V.; Vaxevanopoulos, M. Mines, Metals and money: Ancient world studies in science, archaeology and history. In *Metallurgy in Numismatics*; Sheedy, K.A., Davis, G., Eds.; Royal Numismatic Society Special Publication: London, UK, 2018; Volume 6, pp. 9–21.
35. Melfos, V.; Voudouris, P.C. Geological, mineralogical and geochemical aspects for critical and rare metals in Greece. *Minerals* **2012**, *2*, 300–317. [[CrossRef](#)]
36. Eldorado Gold Corporation 2020, Resources and Reserves. Available online: <https://www.eldoradogold.com/assets/resources-and-reserves/default.aspx> (accessed on 8 December 2020).
37. Melfos, V.; Voudouris, P. Cenozoic metallogeny of Greece and potential for precious, critical and rare metals exploration. *Ore Geol. Rev.* **2017**, *89*, 1030–1057. [[CrossRef](#)]
38. Voudouris, P.; Mavrogonatos, C.; Spry, P.G.; Baker, T.; Melfos, V.; Klemm, R.; Haase, K.; Repstock, A.; Djiba, A.; Bismayer, U.; et al. Porphyry and epithermal deposits in Greece: An overview, new discoveries, and mineralogical constraints on their genesis. *Ore Geol. Rev.* **2019**, *107*, 654–691. [[CrossRef](#)]
39. Goodenough, K.M.; Schilling, J.; Jonsson, E.; Kalvig, P.; Charles, N.; Tuduri, J.; Deady, E.A.; Sadeghi, M.; Schiellerup, H.; Müller, A.; et al. Europe’s rare earth element resource potential: An overview of REE metallogenic provinces and their geodynamic setting. *Ore Geol. Rev.* **2016**, *72*, 838–856. [[CrossRef](#)]
40. Baker, T. Gold±copper endowment and deposit diversity in the Western Tethyan magmatic belt, southeast Europe: Implications for exploration. *Econ. Geol.* **2019**, *114*, 1237–1250. [[CrossRef](#)]
41. Cassard, D.; Bertrand, G.; Billa, M.; Serrano, J.J.; Tourlière, B.; Angel, J.M.; Gaál, G. ProMine mineral databases: New tools to assess primary and secondary mineral resources in Europe. In *3D, 4D and Predictive Modelling of Major Mineral Belts in Europe. Mineral Resource Reviews*; Weihed, P., Ed.; Springer: Cham, Switzerland, 2015; pp. 9–58. [[CrossRef](#)]
42. Stergiou, C.L.; Melfos, V.; Voudouris, P. A review on the critical and rare metals distribution throughout the Vertiskos Unit, N. Greece. In Proceedings of the 1st International Electronic Conference on Mineral Science at Sciforum, Online. 16–31 July 2018; MDPI: Basel, Switzerland. [[CrossRef](#)]
43. Papadopoulos, A.; Tzifas, I.T.; Tsikos, H. The potential for REE and associated critical metals in coastal sand (placer) deposits of Greece: A review. *Minerals* **2019**, *9*, 469. [[CrossRef](#)]
44. Stouraiti, C.; Angelatou, V.; Petushok, S.; Soukis, K.; Eliopoulos, D. Effect of Mineralogy on the Beneficiation of REE from Heavy Mineral Sands: The Case of Nea Peramos, Kavala, Northern Greece. *Minerals* **2020**, *10*, 387. [[CrossRef](#)]
45. Eliopoulos, D.G.; Economou-Eliopoulos, M.; Zelyaskova-Panayiotova, M. Critical factors controlling Pd and Pt potential in porphyry Cu–Au deposits: Evidence from the Balkan Peninsula. *Geosci. J.* **2014**, *4*, 31–49. [[CrossRef](#)]
46. Fornadel, A.P.; Spry, P.G.; Melfos, V.; Vavelidis, M.; Voudouris, P. Is the Palea Kavala Bi–Te–Pb–Sb±Au district, northeastern Greece, a reduced intrusion-related system? *Ore Geol. Rev.* **2011**, *39*, 119–133. [[CrossRef](#)]
47. Voudouris, P. Comparative mineralogical study of Tertiary Te-rich epithermal and porphyry systems in northeastern Greece. *Miner. Petrol.* **2006**, *87*, 24–275. [[CrossRef](#)]
48. Voudouris, P.C.; Spry, P.G.; Mavrogonatos, C.; Sakellaris, G.A.; Bristol, S.K.; Melfos, V.; Fornadel, A.P. Bismuthinite derivatives, lillianite homologues and bismuth sulfotellurides as indicators of gold mineralization in the Stanos shear-zone related deposit, Chalkidiki, Northern Greece. *Canad. Miner.* **2013**, *51*, 119–142. [[CrossRef](#)]
49. Voudouris, P.; Melfos, V.; Spry, P.G.; Kartal, T.; Schleicher, H.; Moritz, R.; Orтели, M. The Pagoni Rachi/Kirki Cu–Mo–Re–Au–Ag–Te deposit, northern Greece: Mineralogical and fluid inclusion constraints on the evolution of a telescoped porphyry-epithermal system. *Canad. Miner.* **2013**, *51*, 411–442. [[CrossRef](#)]

50. Voudouris, P.; Melfos, V.; Spry, P.G.; Bindi, L.; Moritz, R.; Ortelli, M.; Kartal, T. Extremely Re-rich molybdenite from porphyry Cu-Mo-Au prospects in northeastern Greece: Mode of occurrence, causes of enrichment, and implications for gold exploration. *Minerals* **2013**, *3*, 165–191. [[CrossRef](#)]
51. Filippidis, A.; Kougoulis, C.; Michailidis, K. Sr-bearing stilbite in a quartz monzonite from Vathi, Kilkis, Northern Greece. *Schweiz. Mineral. Petrogr. Mitt.* **1988**, *68*, 67–76. [[CrossRef](#)]
52. Frei, R. Isotope (Pb, Rb-Sr,S,O,C,U-Pb) Geochemical Investigations on Tertiary Intrusives and Related Mineralizations in the Serbomacedonian Pb-Zn, Sb+Cu-Mo Metallogenic Province in Northern Greece. Ph.D. Thesis, Swiss Federal Institute of Technology (ETH), Zurich, Switzerland, 1992.
53. Stergiou, C.L.; Melfos, V.; Voudouris, P.; Spry, P.G.; Papadopoulou, L.; Chatzipetros, A.; Giouri, K.; Mavrogonatos, C.; Filippidis, A. The geology, geochemistry, and origin of the porphyry Cu-Au-(Mo) system at Vathi, Serbo-Macedonian Massif, Greece. *Appl. Sci.* **2021**, *11*, 479. [[CrossRef](#)]
54. Kelepertsis, A.E.; Reeves, R.; Andrulakis, J. Geochemical studies of porphyry type mineralization at Gerakario-Vathi of Kilkis area, northern Greece. *Mineral Wealth* **1986**, *42*, 43–48.
55. Kydonakis, K.; Brun, J.P.; Pujol, M.; Monié, P.; Chatzitheodoridis, E. Inferences on the Mesozoic evolution of the North Aegean from the isotopic record of the Chalkidiki blocks. *Tectonophysics* **2016**, *682*, 65–84. [[CrossRef](#)]
56. Siron, C.R.; Rhys, D.; Thompson, J.F.; Baker, T.; Veligrakis, T.; Camacho, A.; Dalampiras, L. Structural controls on porphyry Au-Cu and Au-rich polymetallic carbonate-hosted replacement deposits of the Kassandra mining district, Northern Greece. *Econ. Geol.* **2018**, *113*, 309–345. [[CrossRef](#)]
57. Schmid, S.M.; Fügenschuh, B.; Kounov, A.; Matenco, L.; Nievergelt, P.; Oberhänsli, R.; Pleuger, J.; Schefer, S.; Schuster, R.; Tomljenović, B.; et al. Tectonic units of the Alpine collision zone between Eastern Alps and western Turkey. *Gondwana Res.* **2020**, *78*, 308–374. [[CrossRef](#)]
58. Kiliyas, A.; Falalakis, G.; Mountrakis, D. Cretaceous-Tertiary structures and kinematics of the Serbomacedonian metamorphic rocks and their relation to the exhumation of the Hellenic hinterland (Macedonia, Greece). *Int. J. Earth Sci.* **1999**, *88*, 513–531. [[CrossRef](#)]
59. Mposkos, E.; Krohe, A.; Baziotis, I. Deep tectonics in the Eastern Hellenides uncovered: The record of Variscan continental amalgamation, Permo-Triassic rifting, and Early Alpine collision in Pre-Variscan continental crust in the W-Rhodope (Vertiscos-Ograzden Complex, NGreece). *Tectonics* **2021**, *40*, e2019TC005557. [[CrossRef](#)]
60. Brun, J.P.; Sokoutis, D. Core complex segmentation in North Aegean, a dynamic view. *Tectonics* **2018**, *37*, 1797–1830. [[CrossRef](#)]
61. Tranos, M.D.; Kiliyas, A.A.; Mountrakis, D.M. Geometry and kinematics of the Tertiary post-metamorphic Circum Rhodope Belt Thrust System (CRBTS) Northern Greece. *Bull. Geol. Soc. Greece* **1999**, *33*, 5–16.
62. Abbo, A.; Avigad, D.; Gerdes, A. Crustal evolution of peri-Gondwana crust into present day Europe: The Serbo-Macedonian and Rhodope massifs as a case study. *Lithos* **2019**, *356*, 105295. [[CrossRef](#)]
63. Tsirambides, A.; Filippidis, A. Gold metallogeny of the Serbomacedonian-Rhodope metallogenic belt (SRMB). *Bull. Geol. Soc. Greece* **2016**, *50*, 2037–2046. [[CrossRef](#)]
64. Guillong, M.; Meier, D.L.; Allan, M.M.; Heinrich, C.A.; Yardley, B.W.D. Appendix A6: SILLS: A MATLAB-based program for the reduction of laser ablation ICP-MS data of homogeneous materials and inclusions. In *Laser Ablation ICP-MS in the Earth Sciences: Current Practices and Outstanding Issues*; Sylvester, P., Ed.; Mineralogical Association of Canada Short Course 40: Vancouver, BC, Canada, 2008; pp. 328–333.
65. Rudnick, R.L.; Gao, S. Composition of the continental crust. In *The Crust*, 1st ed.; Rudnick, R.L., Holland, H.D., Turekian, K.K., Eds.; Elsevier: Amsterdam, The Netherlands, 2005; pp. 1–64.
66. Voudouris, P.; Mavrogonatos, C.; Melfos, V.; Spry, P.G.; Magganas, A.; Alfieris, D.; Soukis, K.; Tarantola, A.; Periferakis, A.; Kołodziejczyk, J.; et al. The geology and mineralogy of the Stypsi porphyry Cu-Mo-Au-Re prospect, Lesvos Island, Aegean Sea, Greece. *Ore Geol. Rev.* **2019**, *112*, 103023. [[CrossRef](#)]
67. Voudouris, P.; Spry, P.G.; Melfos, V.; Alfieris, D. Tellurides and bismuth sulfosalts in gold occurrences of Greece: Mineralogical and genetic considerations. In *Gold Deposits in Finland*; Kojonen, K.K., Cook, N.J., Ojala, V.J., Eds.; Geological Survey of Finland: Espoo, Finland, 2007; Volume 53, pp. 85–94.